Use of Computer Vision in μ-Plasma Metal Additive Manufacturing Process for Defect Detection

MTech. Thesis

By

Kartik Chaudhary

Department of Mechanical Engineering

Indian Institute of Technology Indore

June 2025

Use of Computer Vision in μ-Plasma Metal Additive Manufacturing Process for Defect Detection

A THESIS

Submitted in partial fulfillment of the

requirements for the award of the degree

of

Master of Technology

by

Kartik Chaudhary

Discipline of Mechanical Engineering

Indian Institute of Technology Indore

June 2025

Indian Institute of Technology Indore

Candidate's Declaration

I hereby certify that the work which is being presented in the thesis entitled **"Use of Computer Vision in µ-Plasma Metal Additive Manufacturing Process for Defect Detection"** in the partial fulfillment of the requirements for the award of the degree of **Master Of Technology** and submitted in the **Discipline of Mechanical Engineering, Indian Institute of Technology Indore**, is an authentic record of my own work carried out during the time period from **July 2023 to May 2025** under the supervision of **Prof. Neelesh Kumar Jain** (Professor, HAG), Department of Mechanical Engineering, Indian Institute of Technology Indore and **Dr. Sagar Nikam,** Lecturer, School of Computing, Engineering and Intelligent Systems, Ulster University, Derry/ Londonderry, UK. The matter presented in this thesis has not been submitted by me for the award of any other degree of this or any other institute.

Kartik Chaudhary

This is to certify that the above statement made by the candidate is correct to the best of our knowledge.

25th June 2025
Signature of 1st Supervisor of M.Tech. thesis (with date)
(Prof. Neelesh Kumar Jain)

25th June 2025
Signature of 2nd Supervisor of M.Tech. thesis (with date)
(Dr. Sagar H. Nikam)

Kartik Chaudhary has successfully given his M.Tech. Oral Examination held on **26th May 2025**.

Signatures of M.Tech. Thesis Supervisors
Date: **25th June 2025**

Signature of DPGC Convener
Date: 27-06-2025

Abstract

Deposition defects such as discontinuity, non-uniformity, waviness, under-dilution, over-dilution, porosity, balling, spattering, and poor surface quality in the metal additive manufacturing (MAM) processes significantly influence properties and performance of the fabricated product. Waviness and non-uniformity are characterized by unacceptable variations in deposition height and width respectively along the deposition length. The deposition defects reduce strength, toughness, fatigue life, and wear resistance thus making the product unsuitable for the intended application. They lead to metrological inaccuracies in the final product and can even lead to rejection of the entire thus necessitates their expensive post-processing. Therefore, real-time detection and elimination or minimization of the deposition defects is crucial to performance and service of the MAM products and for elimination of the expensive post-processing. This research proposes computer-vision based defect detection methodology to detect discontinuity, non-uniformity, waviness, under-dilution, and over-dilution in µ-Plasma Metal Additive Manufacturing (µ-PMAM) fabricated single-layer depositions of different biocompatible materials using hue saturation value (HSV) based color segmentation and centroid distance and the trained YOLO models. High-quality videos were recorded of single-layer depositions of Ti6Al4V, 63Co29Cr4Mo4Ti, and SS 316L materials using a high dynamic range (HDR) camera mounted on 5-axis CNC machine of µ-PMAM process for different parametric combinations. Images were extracted at rate of one image per second from each recorded video. The extracted images were annotated by the Visual Geometry Group (VGG) image annotator and deposition height and width were extracted from these images using HSV based color segmentation and computation of centroid distance. Discontinuity, non-uniformity, and waviness were detected by plotting the variations in deposition height and width along the deposition length. Subsequently, trained YOLOv8 and YOLOv11 models were used to predict deposition height and width from the unannotated images of SS 316L after training and validating them using annotated images. These models were trained for 50 epochs for different combinations of batch size, image size, and hyperparameters (i.e., learning rate, momentum, and weight decay). The YOLO model predicted deposition height and width were plotted along the deposition length to detect non-uniformity, waviness, under-dilution, and over-dilution. A comparative study of the defects detected by the HSV based approach and YOLO models found superiority of the YOLO models in deposition defect detection of single-layer depositions by µ-PMAM. The proposed defect detection methodology is scalable and can be used for any MAM process and any material because it does not depend on them.

List of Publications

1. **Kartik Chaudhary,** Balbir Singh Negi, Neelesh Kumar Jain, Sagar Nikam, Deepika Nikam, Pradyumn Kumar Arya, *"Use of Computer Vision for Detection of Defects in µ-Plasma Metal Additive Manufacturing Process"* (Submitted to **Progress in Additive Manufacturing**) (**Impact Factor: 4.4**).

2. Anubhav Vaishnav, **Kartik Chaudhary**, Neelesh Kumar Jain, Sagar Nikam, Deepika Nikam, *"Integration of machine learning and computer vision for real-time detection and elimination of defects"* (To be submitted to the **Journal of Intelligent Manufacturing**) (**Impact factor: 5.9**).

3. Sagar Nikam, Raj Agarwal, Akriti Nigam, Neelesh Kumar Jain, **Kartik Chaudhary**, Sonya Coleman, Dermot Kerr, Deepika Nikam, "*AI-Vision based Real-Time in-situ Monitoring of the Metallic Deposition in µ-Plasma Transferred Arc Additive Manufacturing Process."* (To be submitted to the **Additive Manufacturing**) **(Impact Factor: 10.3)**.

Acknowledgements

I take this opportunity to express my deepest sense of respect and gratitude towards my thesis supervisors Prof. Neelesh Kumar Jain and Dr. Sagar Nikam for their trust in me to carry out this work under their supervision. Their constant encouragement and support have enabled this work to achieve its present form. Their innovative stand on things have shaped my perspective and their continuous drive for excellence has motivated me immensely in working to the best of my capabilities and to look for an opportunity in every adverse situation throughout the project. I am also thankful to all the faculties of our Mechanical Engineering Department for supporting and providing us facilities, moral support, and friendly environment throughout this M. Tech program.

I express my deep sense of gratitude to PhD scholars Balbir Singh Negi, Pradyumn Kumar Arya, Rahul Naidu and Ravindra Verma and the lab technicians, Deepak Rathore and Vinay Kumar Mishra for supporting me morally during this journey and technically in handling the sophisticated machines in the laboratory and always maintaining a home-like atmosphere in the lab. Lastly, this project would not have reached to its logical end without the unwavering blessings and moral support of my beloved parents and close friends. I convey my heartfelt gratitude and deepest reverences to them for the successful completion of this dissertation.

Kartik Chaudhary

Dedication

This thesis is dedicated to my parents, for their endless love, unwavering support, and constant encouragement. They believed in me, even when I struggled to believe in myself. I would like to dedicate this thesis to my supervisors. Their guidance, wisdom, and inspiration have shaped my path and helped me grow during this journey.

Table of Contents

List of Figures

List of Tables

Acronyms

3D 3-Dimensional

AM Additive Manufacturing

ASTM American Society for Testing and Materials

CNC Computer Numeric Control

CNN Convolutional Neural Network

CT Computed Tomography

CV Computer Vision

DED Directed Energy Deposition

DSOD Deeply Supervised Object Detectors

DTI Diffusion Tensor Imaging

EB-PBF Electron Beam-Powder Bed Fusion

FCISs Fatigue Crack Initiation Sites

HDR High Dynamic Range

ISO International Organization for Standardization

KNN K- Nearest Neighbour

L-DED Laser- Directed Energy Deposition

L-PBF Laser-Powder Bed Fusion

MIMICS Materialise Interactive Medical Image Control System

ML Machine Learning

MRI Magnetic Resonance Imaging

µ-PMAM Micro -Plasma Metal Additive Manufacturing Process

RO Research Objective

SAPIO Sistema de Aquisição e Processamento de Imagens de Ovitrampa

SVM Support Vector Machine

VGG Visual Geometry Group

YOLO You Only Look Once

Chapter 1

Introduction

This chapter presents brief introduction of computer vision, its advantages and applications, YOLO models, additive manufacturing (AM) and classification of different AM processes, working principle and applications of µ-PMAM process along with the defects produced by it. It ends with providing organization of this thesis.

1.1 Introduction of Computer Vision (CV)

Computer vision (CV) is a field of artificial intelligence that enables machines to interpret, analyze, and extract meaningful data from the images and videos, mimicking human vision and cognitive abilities. It involves high-level understanding, grasping, analyzing, and processing the visual data to extract meaningful information and make useful decisions. Following typical tasks are performed by the CV:

- **Object Classification:** Identification of the defined objects in an image/video, and assigning label to each identified object.
- **Object Localization:** Finding locations of the identified objects in an image/video by enclosing each object in a bounding box.
- **Object Detection:** It is a combination of the object classification and object localization to recognize and locate the defined objects in an image/video. Fig 1.1 shows the object classification, localization, detection, and segmentation tasks by computer vision in a single and multiple objects images.
- **Object Recognition:** It provides an input image to a model through combination of the object classification and object localization and gives the likelihood of the recognized object belonging to a particular class.

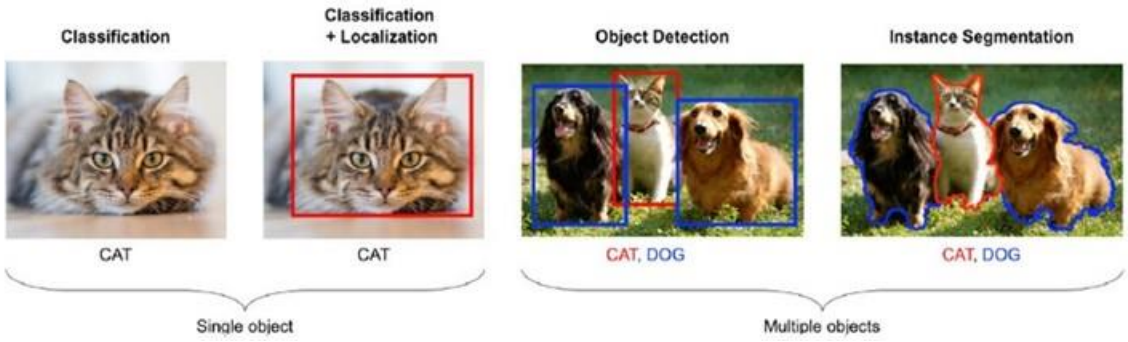

Fig. 1.1: Object classification, localization, detection, and segmentation tasks by computer vision in a single and multiple objects images (**Diwan et *al.* 2023)**.

Object detection by the CV plays a very important role in many applications, such as defect detection in manufacturing, self-driving cars, surveillance, and augmented reality.

Vijayakumar and Vairavasundaram (2024) described use of object detection algorithm in different applications with a particular emphasis on enhancing efficiency and accuracy. State-of-the-art models such as YOLO and Region-based Convolutional Neural Network (R-CNN) are widely employed to provide real-time and robust object detection capabilities. These algorithms find extensive applications in various domains including autonomous vehicles, surveillance systems, smart cities, and healthcare, showcasing their versatility and effectiveness in addressing diverse visual recognition challenges.

1.1.1 Advantages of Computer Vision

Following are some unique advantages of computer vision which make it an effective alternative to the traditional detection techniques:

- **Automated Visual Inspection**: This capability of CV helps to detect defects in assembly lines without human intervention. The CV based self-checkout systems in retail sector are used to automatically identify and bill the products.
- **Speed and Efficiency:** Speed and efficiency of CV help in quick analysis of the X-rays and magnetic resonance imaging (MRI) data aiding in rapid diagnosis of disease thus reducing waiting times of patients. Similarly, multiple cameras for surveillance purposes aid in real-time detection of intrusions or unusual behavior instantly.
- **Cost Reduction**: Automated crop monitoring in large-scale farms using CV decreases operational costs by reducing manual labour. Similarly, computer vision based smart traffic monitoring systems in place of physical traffic controllers help in cutting down the infrastructural expenses.
- **Accuracy and Consistency:** Precise object detection by CV helps in reducing road accidents caused by human carelessness. It also plays a crucial role in quality control of products as it allows consistent quality checks which significantly reduces the producer's and consumer's risk.
- **Safety:** Use of CV systems in the mines act as a safety net to prevent the workers from entering unsafe conditions and/or locations.

1.1.2 Some Domain Specific Applications of Computer Vision

Researchers have explored applications of computer vision in different domains. Following are some examples:

DeCost and Holm (2015) applied computer vision to develop quantitative microstructure descriptors for a diverse collection of microstructure data. For classification of microstructures, support vector machine (SVM) was trained with greater than 80% accuracy over 5-fold cross validation. The developed real-time microstructure descriptors

can capture the meaningful details and define characteristics of microstructural images without explicit fine-tuning from human experts.

Gargiulo et *al*. (2017) used computed tomography (CT), MRI images, and diffusion tensor imaging (DTI) tractography and used image segmentation protocols namely MIMICS to develop 3D model of skull base, tumor, and five eloquent fiber tracts. The developed 3D models were rapid-prototyped and linked with patient images to develop a reported surgical navigation system.

Lin et *al*. (2017) proposed a camera-based line-laser obstacle detection system to prevent the falls of elderly persons in the indoor environment. This system casts a laser line, which passes through a horizontal plane and has a specific height to the ground. A camera, whose optical axis has a specific inclined angle to the plane, observes the laser pattern to obtain the potential obstacles. When obstacles are detected, the system sounds alarm messages to catch the attention of the human beings.

Wang et *al*. (2020) developed a deeply supervised object detector to provide information about the fatigue crack initiation sites which are crucial for fatigue failure investigations of metallic products. They used convolutional neural networks (CNN) to improve the training efficiency of their detector. Their results demonstrated that increasing training dataset size can improve accuracy of CNN while raising the number of epochs can result in its superior ability to recognize the delicate features. Most of the images that cannot be recognized possess common characteristics such as poor image quality, unclear features, and insufficient training data.

Cunha et *al*. (2024) used computer vision to recognize and count dengue mosquito eggs in a trap to control mosquitoes and consequently the dengue fever. The other is a probabilistic model called physiotherapeutic evaluation platform, in which CV was used to aid in visualization of human body balance, by monitoring the center of mass which helps to measure a patient's abdominal strength, assisting the physiotherapist in prescribing exercises aimed at muscle strengthening.

1.2 Introduction of YOLO Model

The traditional object detection models often face limitations in terms of speed because they require multiple scans over an image to identify the objects. These models are region-based, and are computationally intensive which hinder their real-time applications. Whereas, YOLO (*You Only Look Once*) is a pretrained model which belongs to a family of real-time object detection algorithms. A YOLO model is designed to detect and classify objects within an image or video using a unique one-shot detection approach which significantly improves its object detection speed. A YOLO model achieves its impressive

real-time processing capabilities by dividing the entire image into the small grids and making a prediction directly for each grid. This makes it particularly advantageous for the applications requiring swift and accurate identification of objects in dynamic environments. Twelve versions of YOLO model have been launched since their beginning in 2015 as shown in Fig. 1.2. Each version has some improvements over the previous version for better detection performance.

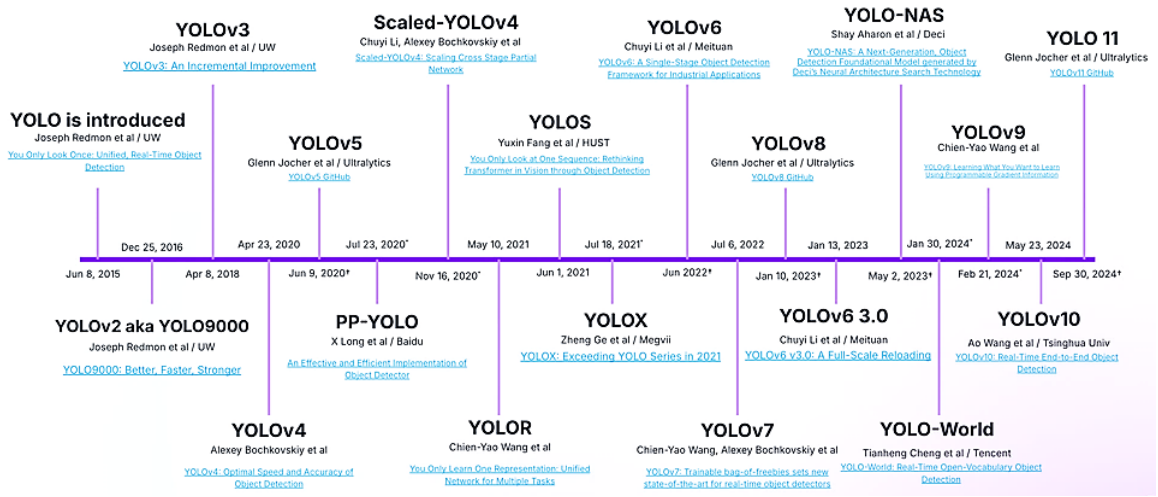

Fig. 1.2: Timeline of launch of different versions of YOLO models.

1.3 Introduction of Additive Manufacturing

Additive manufacturing (AM) is defined by the joint ISO/ASTM terminology standard to be the "process of joining materials to make parts from 3D model data, usually layer upon layer, as opposed to subtractive manufacturing and formative manufacturing methodologies". The pertinent part is the use of a computer to translate a solid model into a real part (**Bourell, 2016)**. AM, often referred to as 3D printing, is a type of digital fabrication technique that builds physical items from a geometrical model through the addition of materials. The field of AM is rapidly expanding. It has been a common practice around the world in recent years. AM has a wide range of applications across various industries such as aerospace, automotive, healthcare, architecture, construction, education, and research. Mass customization and manufacture of open-source designs are becoming increasingly common uses of AM in agricultural, healthcare, automotive, and locomotive industries (**Jadhav and Jadhav, 2022)**.

1.3.1 Classification of AM Processes

According to ASTM F42, different AM processes are categorized into the following seven categories as shown in Fig. 1.3 (**Stavropoulos and Foteinopoulos, 2018)**:

1. Powder Bed Fusion
2. Directed Energy Deposition (DED)

3. Sheet Lamination
4. Binder Jetting
5. Material Jetting
6. Material Extrusion
7. Vat Photopolymerization

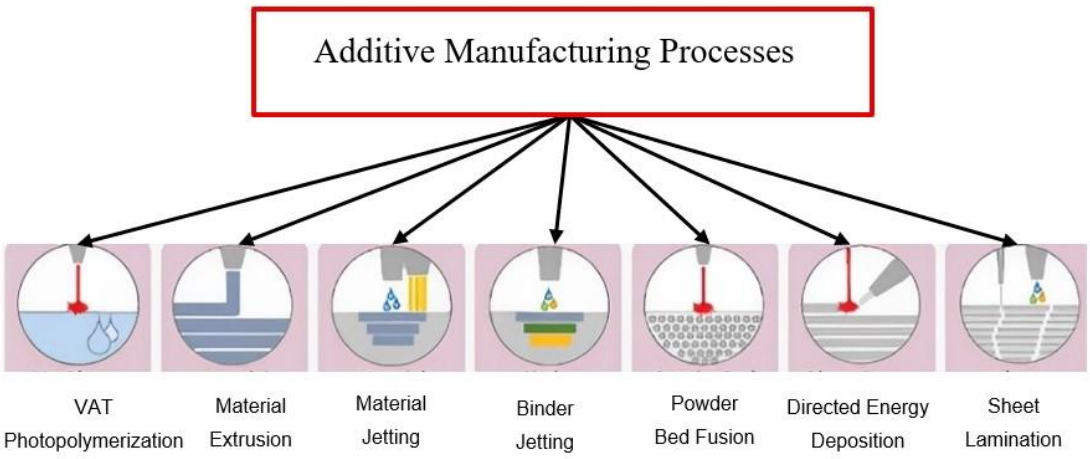

Fig. 1.3: Classification of different types of AM processes according to ASTM F42 **(Wiberg, 2021)**.

- **Powder Bed Fusion (PBF):** PBF type AM processes use heat source in the form a laser or electron beam to selectively fuse regions of the *powdered* bed of the feedstock material which is either metallic material or a polymer. Electron Beam Melting (EBM), Selective Laser Sintering (SLS), Selective Laser Melting (SLM), Direct Metal Laser Sintering (DMLS), Selective Heat Sintering (SHS), and Multi Jet Fusion (MJF) are common AM processes in this category. They differ based on the materials they use and how much melting takes place during the process. The PBF processes have ability to integrate at small scale and they are used for AM of relatively large products. Their machines are of large size. But, built speed is relative slow, they require high µ-plasma power, and their surface finish depends on the powder size.
- **Directed Energy Deposition (DED):** DED type AM processes use the concentrated heat source in the form a laser, electron beam, plasma arc, or µ-plasma arc to melt and fuse the feedstock material as is being deposited. The feedstock material is a metallic material which can be supplied either in powder form or wire form or combination of the both. These AM processes produce high quality functional products, perform precise repair of the existing components, add complex features to the pre-fabricated parts, produce and restore high-value engineering components, and fabricate near-net-shape products. Their build speed is often sacrificed for higher accuracy. The DED fabricated products require post-processing to achieve the desired quality. Laser

Engineering Net Shape (LENS), Laser Metal Deposition (LMD), Wire-arc Additive Manufacturing (WAAM), and µ-plasma Metal Additive Manufacturing (µ-PMAM) are the commonly used DED type AM processes.

- **Sheet Lamination:** Sheet lamination type AM processes bond together the *sheets* or *foils* of different metallic materials, papers or fabrics using heat, adhesives, or ultrasonic waves to supply the required bonding energy. A laser, or milling machine is used to make products from the laminated sheets. Laminated Object Manufacturing (LOM) and Ultrasonic Additive Manufacturing (UAM) are the commonly used sheet lamination type AM processes. These processes offer high build speed, low cost, ease of material handling, higher accuracy, and good finish.
- **Binder Jetting:** In binder jetting type AM processes, a liquid bonding agent is selectively deposited to join *powder* of feedstock material (either a metallic material or a polymer) thus binding them to create a solid layer. When one layer is finished, the platform moves down, and new powder is added on top. This cycle repeats until the full object is completely built. Powder Bed and Inkjet Head (PBIH) and Plaster-based 3D Printing (PP) are the commonly used binder jetting type AM processes. Advantages of these processes include: faster process, high range of materials, allows use of two materials, use of different colours. Their major limitations are: not always suitable for structural parts due to use of binder material, and higher amount of post processing
- **Material Jetting:** Material jetting involves depositing *droplets* of the feedstock material (usually photopolymers or waxes) onto a build platform, where they are immediately solidified by UV light. This process is similar inkjet printing in 3D. Advantages of material jetting type AM processes include: high accuracy, less wastage of materials, ability to fabricate multi-materials and multi-colours products thus making them ideal for visual prototypes and biomedical models. But they require support structures and are applicable to limited range of materials only. Multi-jet Modelling (MJM) is the most commonly used material jetting type AM process.
- **Material Extrusion:** This process uses a nozzle or orifice to selectively extrude the feedstock material to form its layers. The nozzle moves along the x and y axes to deposit material onto a base, while the platform shifts along the z-axis to create the product layer by layer. Common materials feedstock materials are thermoplastics or thermoplastic composites. It is used to fabricate inexpensive parts from ABS or some other plastics, Extrusion type AM processes are relatively inexpensive, suitable for the visual models and prototypes. But they have low accuracy, small build speed, limited

nozzle radius, requires constant pressure of the feedstock material. Fused Deposition Modelling (FDM) is the most commonly used material extrusion type AM process.

- **Vat Photopolymerization:** This type of AM processes selectively cure a *liquid* photopolymer by exposing it to the light from a laser or projector to produce its solid layers via light-activated polymerization process. The build platform begins at the bottom of a container filled with liquid photopolymer. A light source hardens it based on its cross-section being exposed, solidifying it as it moves up. Stereolithography apparatus (SLA) and Digital Light Processing (DLP) are the commonly used vat polymerization processes. These processes are relatively quick and typically build large areas. But, they are relatively expensive, requires support structure, require higher post-processing time and cost, and are applicable to limited material i.e. photopolymers only.

1.4 Introduction of µ-PMAM Process

The µ-Plasma Metal Additive Manufacturing (µ-PMAM) process is a novel and energy-efficient metal AM (MAM) process that combines the principles of µ-plasma arc with the precision of modern material deposition methods. It represents a significant advancement in the field of DED, especially in applications that demand fine control, and minimal thermal impact. By using µ-plasma arc as low-energy, highly concentrated thermal source as the heat source, µ-PMAM is capable of producing high-quality components from high-melting point metallic materials. The µ-plasma arc is generated inside a specially designed nozzle unlike the plasma arc additive manufacturing (PAAM) process. The nozzle controls the arc size and intensity, ensuring focused heating and efficient material deposition. Unlike conventional PAAM process, µ-PMAM operates at lower µ-plasma current and µ-plasma power levels, usually up to 20 A and 440 W direct current (DC) µ-plasma power. These controlled energy settings offer several benefits, such as reduced heat-affected zones, minimized thermal distortion, and lower residual stresses within the deposited layers. One of the distinguishing features of µ-PMAM process is its integration with 5-axis computer numerically controlled (CNC) work table. Fig. 1.4 depicts photograph of the 5-axis CNC machine for µ-PMAM process showing the deposition head and formation of µ-plasma arc inside the µ-plasma torch in the insets. This configuration allows for the fabrication of geometrically complex parts without any support material. The multi-axis motion enables the deposition head to be programmed for the desired part geometry thus allowing overhangs, internal features, and curved geometries to be manufactured more easily. Consequently, µ-PMAM offers superior flexibility and freedom in part design, reducing the need for post-processing and support

removal. A major advantage of µ-PMAM lies in its compatibility with multiple feedstock forms including powders, wires, or their combinations. This versatility allows users to select the most appropriate form of feedstock material based on part requirements, desired deposition rate, or economic considerations. For instance, powder feedstock offers better control over composition and microstructure, while wire feedstock provides better material utilization and reduced contamination risk. From a materials perspective, µ-PMAM is highly capable of handling a broad range of high-performance and high-melting-point alloys, many of which are difficult to process by other AM processes. The µ-PMAM process has been successfully used for Inconel 625 for high-temperature aerospace applications, P20 and H13 tool steels for mould and die production, and Stellite alloy for wear-resistant surfaces, Ti6Al4V, Co-Cr-Mo-xTi, Ti-Ta-Zr-W-Mo HEA for biomedical implants, and Ti6Al4VxNiyCr alloys for high strength applications. The precise control over heat input and deposition rate allows for stable melting and solidification of challenging materials which helps to expand its material applications. These materials are selected for their mechanical and biological properties, making them ideal for implants, surgical instruments, and prosthetic components.

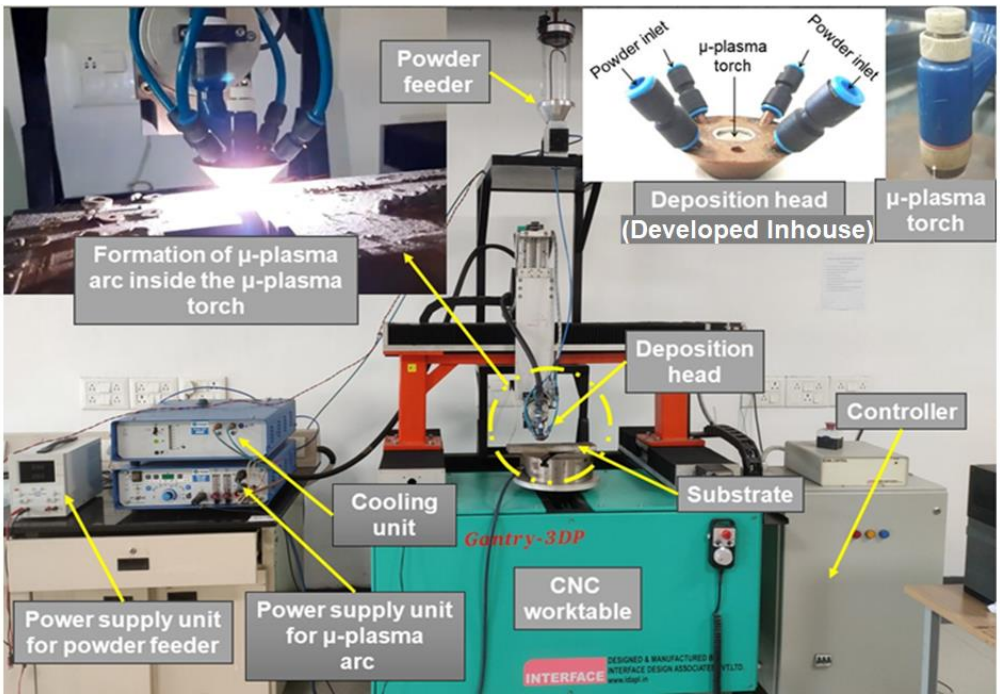

Fig. 1.4: Photograph of the 5-axis CNC machine for µ-PMAM process showing with the insets showing deposition head and formation of µ-plasma arc inside the µ-plasma torch (**Arya et *al*. 2024).**

In terms of functional outcomes, the parts produced through µ-PMAM often exhibit fine-grained microstructures, uniform layer bonding, and high mechanical strength due to controlled thermal cycles and precise deposition paths. Its ability to handle custom

geometries and specialized materials opens new possibilities for repairing, re-manufacturing, and customizing critical components. This is especially relevant in high-value sectors namely aerospace, automotive, biomedical, and defence where performance, reliability, and material efficiency are critical.

1.4.1 Applications of µ-PMAM Process

The µ-PMAM process has been successfully used for processing many high melting point materials. The applications of µ-PMAM process are as follows:

- **Aerospace components:** µ-PMAM enables fabrication of complex, lightweight parts using high-temperature alloys such as Inconel 625, offering superior heat resistance, geometric precision, and reduced material wastage for turbine blades and aerospace brackets.
- **Tools and dies manufacturing:** The µ-PMAM process efficiently produces and repairs moulds of P20 and H13 materials enhancing their useful life, reducing lead time.
- **Biomedical implants and devices:** The µ-PMAM process has been used to process biocompatible materials such as Ti6Al4V, Co-Cr-Mo-xTi, Ti-Ta-Zr-W-Mo with tailored microstructures, allowing the production of patient-specific implants and surgical tools with improved mechanical and biological performance.
- **Development of high-entropy alloy:** The µ-PMAM process has been used to develop advanced alloys such as Ti6Al4VxNiyCr, Co-Cr-Mo-xTi, Ti-Ta-Zr-W-Mo, enabling components with superior strength, corrosion resistance, and biocompatibility for demanding structural and biomedical applications.
- **Component repair and remanufacturing:** µ-PMAM process can repair worn or damaged high-value metallic parts by adding material only where needed, extending component life and reducing replacement costs and environmental waste.

1.4.2 Defects in Depositions by µ-PMAM Process

Despite several advantages offered by µ-PMAM process, **Kumar and Jain (2020)** have highlighted occurrence of the following defects in the depositions fabricated by µ-PMAM process. Some of these defects are shown in Fig. 1.5 for different forms of the feedstock material i.e., powdered form (Fig. 1.5a); wire form (Fig. 1.5b); combined powder-wire form (Fig. 1.5c)

- **Porosity**: It refers to presence of small voids or pores on the surface of the additively manufacturing metallic component as shown in Figs. 1.5a-1.5c. It can occur between the deposition layers (inter-layer porosity shown in Fig. 1.5d1), within a deposition layer (intralayer porosity depicted in Fig. 1.5d2), or between deposition tracks (inter-

track or inter-run porosity illustrated in Fig. 1.5d3). Porosity is a critical quality concern especially for the functional or load-bearing components.

- **Balling:** It is a common defect where the molten material forms discrete spherical droplets instead of a smooth and continuous deposition. It disrupts deposition layer adhesion and compromises the part quality as shown in Fig. Figs. 1.5a-1.5c.
- **Spattering:** It refers to ejection of small molten material droplets from the melt pool as depicted in Figs. 1.5a-1.5c. These spattered particles can land on nearby surfaces or the build itself causing surface defects and poor surface quality porosity, or even delamination in subsequent layers.
- **Wire Inclusion:** This defect is caused when an unmelted or partially melted wire of the feedstock material is embedded within a deposition as shown in Fig. 1.5b.
- **Discontinuity:** It indicates absence of feedstock material at certain locations along the deposition length implying that deposition height and/or deposition width being equal to zero at such locations.
- **Non-uniformity:** It is characterized by unacceptable variations in deposition width along the deposition length as shown in Fig. 1.5f.
- **Waviness:** It is characterized by unacceptable variations or ripples in deposition height along the deposition length.
- **Over-dilution**: It occurs when diluted area is much larger than the deposition area as shown in Fig. 1.5g. It is caused due to the aspect ratio (i.e., ratio of deposition width to deposition height) being greater than its optimum range.
- **Under-dilution**: It is just opposite to over-dilution. It occurs when diluted area is much smaller than the deposition area as shown in Fig. 1.5h. It is due to the aspect ratio (i.e., ratio of deposition width to deposition height) being smaller than its optimum range.
- **Surface Roughness:** It is the measured roughness of functional surface of an AM fabricated component. There are many measures of surface roughness such as arithmetical average roughness *'Ra'* value concept depicted for a multi-layer deposition in Fig. 1.5i), maximum surface roughness *'Rmax'* or *'Ry'* value, ten-spot average roughness *'Rz'* value. They can be measured using standard surface roughness measuring equipment. **Kumar and Jain (2022)** used K-nearest neighbors (KNN) algorithm to predict the surface roughness of the components manufactured by µ-PMAM process.

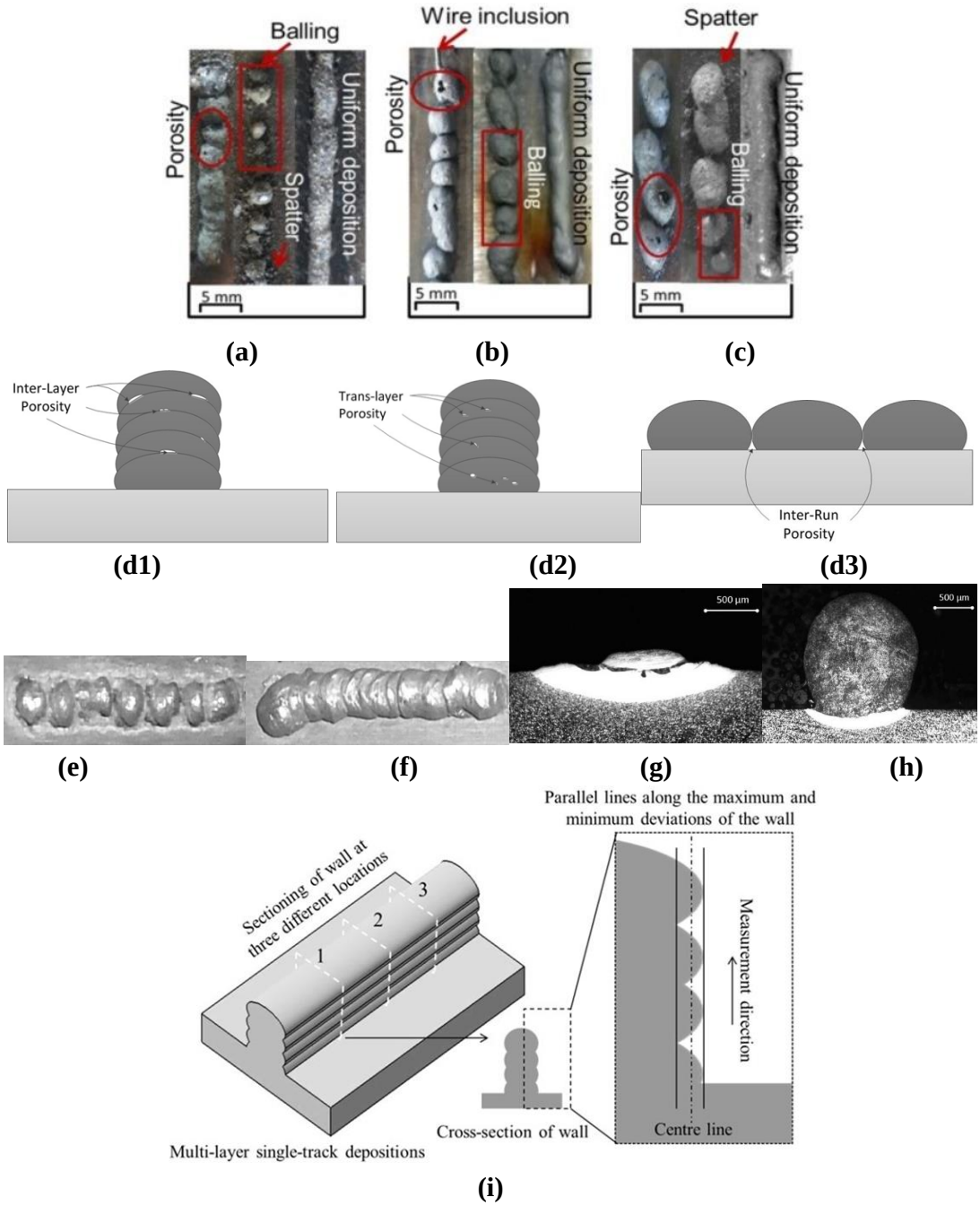

Fig. 1.5: Different deposition defects (a, b, c) porosity, balling, spatter for (a) powder form, (b) wire form, (c) combined powder and wire form, (b) wire inclusion in wire form of feedstock material (**Kumar and Jain, 2020**), (d1) inter-layer porosity, (d2) intralayer porosity, (d3) inter-track or inter-run porosity, (e) discontinuity, (g) non-uniformity, (g) over-dilution, (h) under-dilution (**Jhavar et *al.*, 2016**), and (i) concept of evaluation of average surface roughness 'Ra' value for a multi-layer deposition (**Kumar and Jain, 2022**).

1.5 Organization of Thesis

This thesis is organized into the following five chapters:

Chapter 1 presents brief introduction of computer vision, its advantages and applications, YOLO models, additive manufacturing processes and their classification, working principle and applications of µ-PMAM process along with the defects produced by it. It ends with providing organization of this thesis.

Chapter 2 describes review of the past work done on using computer vision for detection of the defects produced by different AM processes, and detection of defects produced by µ-PMAM process, followed by brief review summary of the past works, identified research gaps, and research objectives along with methodology used to meet them.

Chapter 3 provides details of data acquisition for the present work through high quality recording of videos of single-layer depositions of 63Co29Cr4Mo4Ti, Ti6Al4V, and SS 316L by µ-PMAM process using high dynamic range (HDR) camera. It also presents details of extraction of images from each recorded video, annotation of clearly visible extracted images, proposed deposition defect detection methodology, and methodology for defect detection using HSV based color segmentation and centroid distance and YOLO models.

Chapter 4 provides the results and discussion of this research work by describing the analysis of the deposition defects detected by HSV segmentation and centroid distance and the trained YOLO models in single-layer depositions of SS 316L, Ti6Al4V, and 63Co29Cr4Mo4Ti alloys. It also provides comparison of the ranges for deposition height, deposition width, and aspect ratio identified by HSV-based approach and the trained YOLO models and µ-PMAM process parameters identified by HSV-based approach for continuous, uniform, and non-wavy depositions of the considered materials.

Chapter 5 summarizes the outcome of the present research by presenting its significant achievements, conclusions, and some directions for the future work.

This chapter presented brief introduction of computer vision, its advantages and applications, YOLO models, additive manufacturing processes and their classification, working principle and applications of µ-PMAM process along with the defects produced by it, and organization of this thesis. The **next chapter** review of the past work done on using computer vision for detection of the defects produced by different AM processes, and detection of defects produced by µ-PMAM process, followed by brief review summary of the past works, identified research gaps, and research objectives along with methodology used to meet them.

Chapter 2

Review of Past Work

This **chapter** describes review of the past work done on using computer vision for detection of the defects produced by different AM processes, and detection of defects produced by μ-PMAM process, followed by brief review summary of the past works, identified research gaps, and research objectives along with methodology used to meet them.

2.1 Use of Computer Vision for Detection of AM Defects

Additive manufacturing (AM) processes are known for their design and fabrication flexibility, cost-effectiveness, and high customization. But products manufactured by the AM processes possess many defects such as porosity, balling, discontinuity, non-uniformity, waviness, over-dilution, under-dilution, spattering, delamination of deposition layers in multi-layer deposition, poor surface quality, and poor dimensional and geometrical tolerances. These defect causes poor appearance, properties, and performance of the AM products which make them unsuitable to meet the efficiency and quality requirements of modern production systems. The traditional method to detect these defects is the visual inspection and measurement but it is skilled manpower-intensive and time-consuming process which often results in inaccurate detection of defects and even non-detection of many defects. This leads sheer wastage of time, efforts, and money. Therefore, development of a real-time defect detection methodology for the AM processes is urgently needed to realize them as an established manufacturing technology and computer vision can play an important role in it. Computer vision is a field of artificial intelligence that enables machines to interpret, analyze, and extract meaningful data from the images and videos, mimicking human vision and cognitive abilities. It involves high-level understanding, grasping, analyzing, and processing the visual data to extract meaningful information and make useful decisions. Computer vision has potential to automate defect detection on real-time basis with improved accuracy and efficiency thus making it particularly suitable in large-scale and long-term industrial production processes. It only requires a hardware and a high-end camera for deploying on it for capturing video/images on real-time basis for any future use. Common defect detection methods based on computer vision include thresholding, edge detection, feature extraction, and description. Following paragraph describe the past work done on AM defect detection using computer vision.

Scime and Beuth (2018) used computer vision for in-situ monitoring and analysis to automatically detect and classify the defects that occurred during the powder spreading

while fabricating depositions of SS 316L by laser powder bed fusion (LPBF) process. The defect detection and classification were implemented using an unsupervised machine learning (ML) algorithm, operating on a moderately-sized training database of images. **Scime et *al*. (2020)** used the CNN for pixel-wise segmentation of layer-wise powder bed image data in (i) deposition of Ti6Al4V, AlSi10Mg, Inconel 718, stainless steel 316L, and bronze by LPBF process, (ii) deposition of B_4C and SiC by electron powder bed fusion (EBPF) process, and (iii) deposition of Ti6Al4V by binder jetting type AM process. They detected defects such as porosity spattering, incomplete spreading, and debris. They highlighted that key advantage of CNN algorithm is returning segmentation results at the native resolution of the imaging sensor, seamlessly transferring learned knowledge between different AM machines, as the training data for any individual machine may be limited, knowledge learned on data from one AM machine must be rapidly transferrable across technologies between entirely different powder bed machines and imaging systems and providing real-time performance. **Charalampous et *al*. (2021)** used computer vision-based method to automatically scan, filter, segment, reconstruct, and correlate high-resolution point cloud data of a part fabricated by fused filament fabrication (FFF) process with its digital 3D model to evaluate the process performance. They also experimentally validated effectiveness of their monitoring and defect detection methodology. **Zhang et *al*. (2022)** reviewed in-situ and real-time monitoring of LPBF and laser directed energy deposition (LDED) processes using traditional image processing such as image transformation, recognition, segmentation, and enhancement for analysis of monitoring and classification of the objects. They proposed a technical route for real-time feedback control of metal AM (MAM) processes by combining image processing with AM technologies. They also analyzed problems in image processing, algorithm generalization, quality, small samples, and image labeling. **Nguyen et *al*. (2023)** used a semi-supervised ML algorithm to detect defects in deposition of SS 316L by LPBF process. The ML algorithm was trained to classify the surface appearances as the post-process characteristics, e.g. surface roughness, morphology, or tensile strength in the monitoring data. This approach was validated by performing predictions on test samples having various geometries. **Wang et *al*. (2023)** proposed an enhanced YOLOv8 model to train a defect detection model capable of identifying and evaluating defect images based on four defect categories namely scratches, holes, over-extrusion, and impurities in an extrusion type AM process.

2.2 Detection of Defects in µ-PMAM Process

Kumar and Jain (2020) showed occurrence of porosity, balling, spatter, and wire inclusion through microscopic examination of the Stellite depositions by µ-PMAM process while it in powder form, wire form, and combined powder-wire form. **Kumar and Jain (2022)** used KNN algorithm to predict the surface roughness produced by µ-PMAM process. The surface roughness data for training the KNN algorithm were generated by depositing multi-layer single-track depositions of Stellite-6 in powder and wire form. They reported that surface roughness increased with an increase in µ-plasma power and feedstock material feed rate and decreased with an increase in deposition head traverse rate for both powder and wire form of feedstock material.

2.3 Review Summary of Past Work

It can be summarized from the review of the limited past work available that (i) computer vision has been successfully used via in-situ monitoring to detect the defects in the depositions of Ti6Al4V, AlSi10Mg, Inconel 718, SS 316L, bronze, B_4C, and SiC produced by different AM processes namely LPBF, EPBF, LDED, FFF, and Binder Jetting AM processes. The captured videos/images were carefully processed, analyzed and used to perform these tasks, (ii) Depositions of Stellite by µ-PMAM process revealed occurrence of porosity, balling, spatter, and wire inclusion for its powder, wire, and combined powder-wire form, and (iii) Surface roughness produced by µ-PMAM process has been successfully predicted by using KNN algorithm.

2.4 Identified Research Gaps and Research Objectives

Following are the research gaps identified from the past work review:

- Some work is available on computer vision based real-time detection of the defects in LPBF, EPBF, LDED, FFF, Binder Jetting type AM processes during depositions of Ti6Al4V, AlSi10Mg, SS 316L, Inconel 718, Bronze, B_4C, and SiC.
- Limited work is available on post-process detection of defects and KNN based surface roughness prediction in the metallic depositions made by the µ-PMAM process.
- No work is available on computer vision based real-time detection of defects such as discontinuity, non-uniformity, waviness, under-dilution, over-dilution in the depositions of biocompatible metallic materials (such as 63Co29Cr4Mo4Ti, Ti6Al4V, and SS 316L) fabricated by the µ-PMAM process.

Based upon the review of the past work and its above-mentioned summary, following research objectives were identified for the present work:

- **RO-1:** Recording of high-quality videos of single-layer depositions of three biocompatible metallic materials (namely 63Co29Cr4Mo4Ti, Ti6Al4V, and SS 316L) produced by the µ-PMAM process. Extraction of images from each recorded video and making them clearly visible via segregation and preprocessing. Annotation of the extracted clearly visible images by the Visual Geometry Group (VGG) annotator.
- **RO-2:** Computation of deposition width and deposition height from the annotated images using Hue Saturation Value (HSV) based colour segmentation and computing the centroid distance. Detection of discontinuity, non-uniformity, waviness, over-dilution, under-dilution by plotting the variations in *computed* deposition height, deposition width, and aspect ratio along the deposition length.
- **RO-3:** Training and validation of YOLOv8 and YOLOv11 models using the annotated images and their unannotated version. Testing of the trained YOLOv8 and YOLOv11 models using the unannotated images. Prediction of deposition height, deposition width, and computation of aspect ratio by the trained YOLO models. Detection of non-uniformity, waviness, over-dilution, under-dilution by plotting the variations in *predicted* deposition height, deposition width, and computed aspect ratio along the deposition length
- **RO-4:** Comparison of ranges for deposition height, deposition width, and aspect ratio identified by HSV and centroid distance approach and the trained YOLO models. Identification of µ-PMAM process parameters by HSV and centroid distance approach for continuous, uniform, and non-wavy depositions.

2.5 Research Methodology

Fig. 2.1. depicts the methodology used to meet to the identified research objectives of the present work. It starts with recording of high-quality videos of single-layer depositions of 63Co29Cr4Mo4Ti, Ti6Al4V, and SS 316L fabricated by the µ-PMAM process using a high dynamic range (HDR) camera that moves along with the deposition head. Images are extracted from each recorded video followed by annotation of 90% of the clearly visible images (i.e., segregated and pre-processed) by the VGG image annotator. Thereafter, following two approaches were used to detect the defects: approach-1 based on HSV based color segmentation and centroid distance and approach-2 based on YOLO models. Approch-1 *computed* deposition height, deposition width, and aspect ratio and plots of their variations along the deposition length were used to detect discontinuity, non-uniformity, waviness, over-dilution, and under-dilution of the considered depositions. Whereas, approach-2 involved training and validation of YOLOv8 and YOLOv11 models using the annotated images and their unannotated version and their testing using the

unannotated images. Then the trained YOLO models were used to predict deposition height and width. The plots of the variations in the *predicted* deposition height and width, and computed aspect ratio were used to detect non-uniformity, waviness, over-dilution, and under-dilution of the considered depositions. The methodology ends with comparison of ranges for deposition height, deposition width, and aspect ratio identified by both the approaches and identification of μ-PMAM process parameters by the approach-1 for continuous, uniform, and non-wavy depositions of the considered materials.

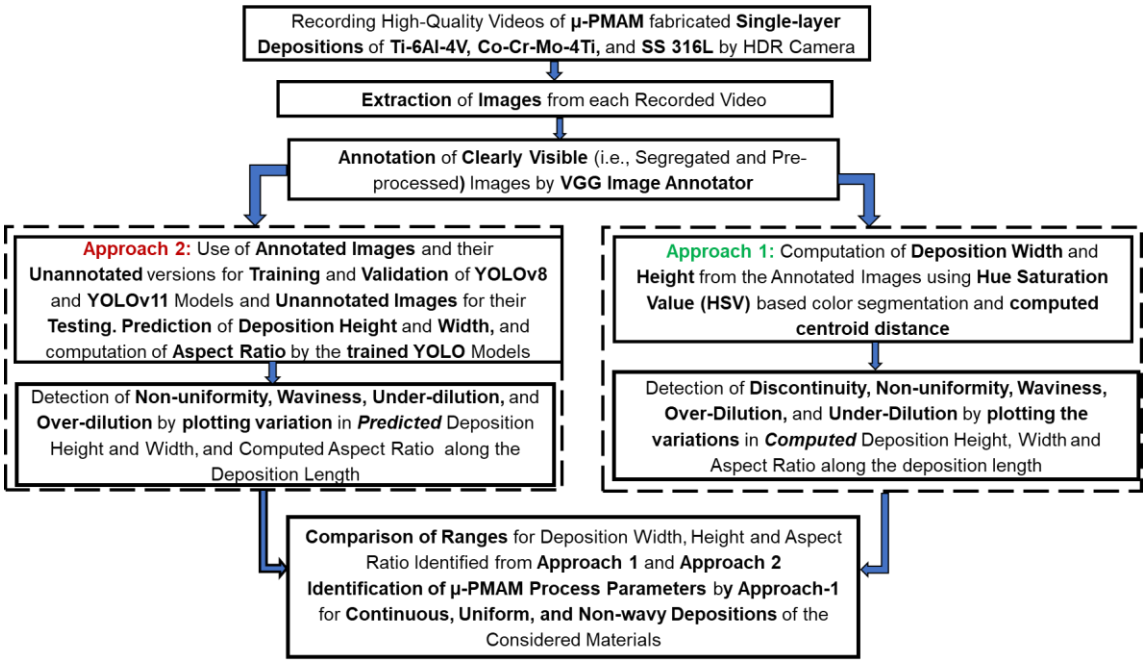

Fig. 2.1: Research methodology used in the present work.

This chapter described review of the past work done on using computer vision for detection of the defects produced by different AM processes, and detection of defects produced by μ-PMAM process, followed by brief review summary of the past works, identified research gaps, and research objectives along with methodology used to meet them. The **next chapter** highlights the different details with regards to the materials and methodologies employed in the analysis of μ-PMAM process.

Chapter 3

Materials and Methods

This chapter provides details of data acquisition for the present work through high quality recording of videos of single-layer depositions of 63Co29Cr4Mo4Ti, Ti6Al4V, and SS 316L by µ-PMAM process using high dynamic range (HDR) camera. It also presents details of extraction of images from each recorded video, annotation of clearly visible extracted images, proposed deposition defect detection methodology, and methodology for defect detection using HSV based color segmentation and centroid distance and YOLO models.

3.1 Data Acquisition

Data in the present work were acquired through recording of high-quality videos of single-layer depositions of three biocompatible materials namely 63Co29Cr4Mo4Ti, Ti6Al4V, and SS 316L by the µ-PMAM process using a HDR camera. Following sections describe details of associated with the data acquisition in the present work.

3.1.1 Selection of Materials

Table 3.1 presents details of the feedstock and base plate materials used for fabricating single-layer depositions by µ-PMAM process.

Table 3.1: Feedstock and base plate materials used in single-layer depositions by µ-PMAM process.

Feedstock material	Base plate material
63Co29Cr4Mo4Ti	Ti6Al4V
Ti6Al4V	Ti6Al4V and mild steel
SS 316L	Mild steel (MS)

Following are justifications for selection of the feedstock materials. The 63Co29Cr4Mo4Ti alloy is known for excellent mechanical strength, corrosion resistance, wear resistance, and biocompatibility making it particularly useful in biomedical engineering applications. Following are its main applications: (i) Knee and hip implants, (ii) Customized dental implants, (ii) Biomedical accessories such as plates, screws, and joining parts, and (iv) Bio-functional coatings due to its improved oxide layer formation which enhances surface stability. The Ti6Al4V, sometimes also called TC4 or Ti64 , is an alpha-beta titanium alloy of ASTM Grade 5. Its composition by wt.% is: 5.5-6.75% Al; 3.5-4.5% V; 0.3% Fe; 0.2%O; 0.08% C; 0.05% N; 0.015%H; and balance Ti. It has excellent biocompatibility, excellent corrosion resistance to seawater, oxidizing acids

and rocket propellants, relatively low density and thermal conductivity, high strength and modulus of elasticity, and good fatigue strength and formability. It is primarily used in various aerospace applications, orthopaedic implants because it promotes bone regeneration, and high-temperature components. The SS 316L is an austenitic stainless steel whose composition by wt.% is: 16-18% Cr; 10-14% Ni; 2-3% Mo; Max. 0.03% C; and small amounts of manganese, silicon, and other elements. The 'L' indicates very less carbon content. It has excellent resistance to atmospheric corrosion, moderately oxidizing and reducing environments, chloride-rich environments, good strength and toughness, even at cryogenic temperatures, good weldability. Its main applications include: (i) Biomedical devices due to its biocompatibility and resistance to corrosion, (ii) Marine environments for structural components and equipment exposed to seawater, (iii) Food processing equipment due to its resistance to corrosion and non-toxicity, (iv) Chemical and petrochemical industries for equipment handling corrosive chemicals, and (v) Cryogenic applications due to its ability to maintain strength at very low temperatures.

The received powders of SS 316L and Ti6Al4V were used for their single-layer depositions whereas powder of 63Co29Cr4Mo4Ti was prepared by mixing the procured powders of Co, Cr, Mo, and Ti in a planetary ball milling machine (*Pulverisette* 6 from *Fritsch, Germany*) in the desired ratio by wt.%. The as received powders had purity of 99.5% and particle size in the range of 45 to 105 µm. The mixing was carried out for 20 hours at 250 rpm using tungsten carbide balls of 15 mm diameter and maintaining ball to powder ratio as 10:1. The powders of 63Co29Cr4Mo4Ti, Ti6Al4V, and SS 316L were de-moisturized for 2 hours in an oven at 80ºC and then were vacuum sealed before their depositions by µ-PMAM process.

3.1.2 Selection of Input Parameters of µ-PMAM Process

Performance of the µ-PMAM process depends on its input parameters. These parameters directly influence the deposition height and width, and consistency of the depositions. Different combinations of the following input parameters were used during video recording of the single-layer depositions of the three materials:

- **µ-plasma power:** It is the energy supplied for formation µ-plasma arc inside the µ-plasma torch. It affects the time required to melt a feedstock material and form a cohesive deposition layer. Higher the µ-plasma power, lesser is the time needed to melt a feedstock material.
- **Feedstock powder flow rate:** It is the rate at which the feedstock material is delivered to the base plate. It influences height and width of a deposition. It depends on density, particle size and sticking tendency of the feedstock powder. Its value is restricted by µ-

plasma power i.e., smaller value of µ-plasma power does not allow use of larger value of feedstock powder flow rate.

- **Deposition head traverse rate:** It is speed at which the deposition head travels over the base plate. Its value is affected by melting point of the feedstock material and µ-plasma power. Higher melting of the feedstock material and/or smaller value of µ-plasma power necessitates small traverse rate of deposition head and vice-versa. It affects geometry of a deposition layer and overall deposition quality.

3.1.3 Recording Videos of Single-Layer Depositions

Fig. 3.1 shows the HDR camera (*Make: TPS; Model: XVC-1000*) mounted on the in-house built 5-axis CNC machine for µ-PMAM process such that it moves along with the deposition head. This HDR camera was selected for its ability to capture high-resolution video which enhances the lighting sensitivity. Video recording of the deposition process at a high image rate made it possible to observe the deposition geometry parameters in real-time and capture any variations that influence the defects. Following 27 black and white videos were recorded using the *XIRIS* software: (i) 15 videos of single-layer depositions of 63Co29Cr4Mo4Ti on Ti6Al4V base plate, (ii) 3 videos of single-layer deposition of Ti6Al4V on same material base plate and 1 video of its single-layer deposition on MS base plate and, (iii) 8 videos for single-layer depositions of SS 316L on MS base plate. Table 3.2 presents details of the recorded videos along with values of µ-PMAM process parameters used in them and number of clearly visible extracted images from each recorded video.

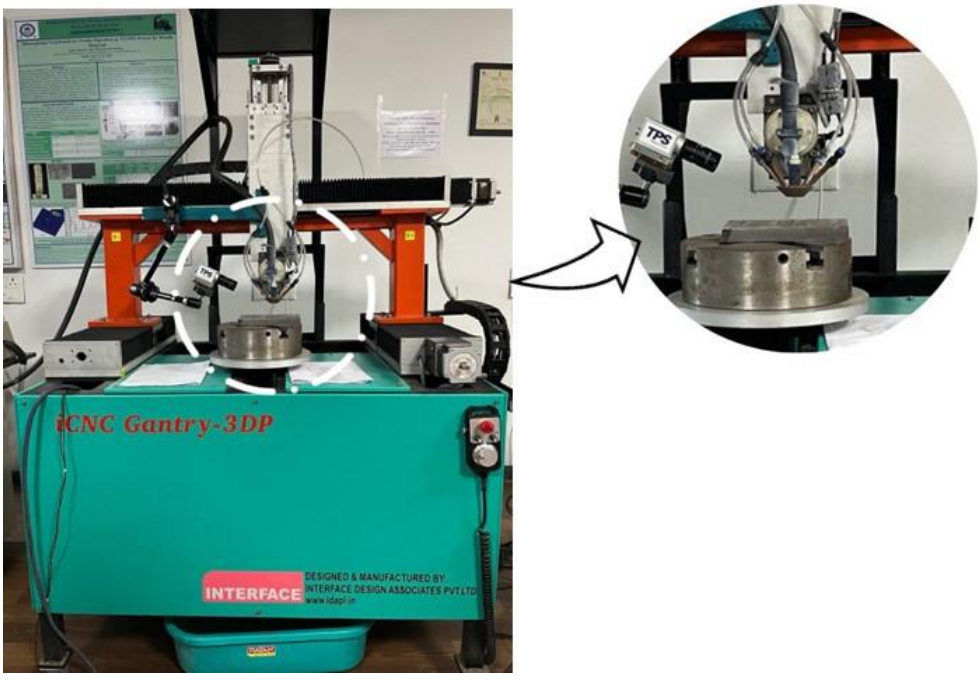

Fig. 3.1: Photograph of the 5-axis CNC machine of µ-PMAM process showing mounting of the HDR camera for recording videos of single-layer depositions.

Table 3.2: Details of the recorded videos for single-layer depositions of 63Co29Cr4Mo4Ti, Ti6Al4V, and SS 316L along with values of µ-PMAM process parameters used in them and number of extracted images from each recorded video.

Video No.	Feedstock material	Substrate material	µ-plasma current (A)	Deposition head traverse speed (mm/min)	Feedstock powder feed rate (g/min)	Video duration (s)	No. of clearly visible extracted images
1	63Co29Cr4Mo4Ti	Ti6Al4V	12	40	2.0	66	470
2			12	45	2.0	71	570
3			12	50	3.0	72	410
4			13	40	2.0	70	510
5			13	45	2.5	48	360
6			13	50	2.0	47	290
7			14	40	2.5	75	430
8			17	30	2.5	93	720
9			17	35	3.0	53	300
10			17	45	2.0	73	530
11			17.5	30	2.0	105	810
12			17.5	35	2.5	86	710
13			18	35	2.0	70	520
14			18	40	3.0	76	640
15			18	45	2.0	60	460
1	Ti6Al4V	Ti6Al4V	15	50	1.7	56	430
2			15	55	3.5	59	510
3			17	50	2.3	80	300
4		Mild steel	15	55	1.5	60	310
1	SS 316L	Mild steel	14	47	1.7	66	600
2			14	50	2.1	54	480
3			14	53	3.5	62	490
4			14.5	47	2.5	71	640
5			14.5	53	2.1	62	520
6			15	47	1.5	69	590
7			15	50	1.7	68	600
8			15	53	1.9	61	520

3.2 Extraction of Images from the Recorded Videos

The algorithm *OpenCV* was used to extract the images at the rate of 10 images per second (ips) from a recorded video of a deposition. It starts with opening of the recorded video file, and finding out its duration and its speed in terms of its ips. Then it computes the time interval between the two consecutive images i.e., an extraction rate of 10 ips will extract an image after every 0.1 second. It is followed by saving the extracted images in an output folder by naming them according to the sequence of their extraction. It ensures that the files of the extracted images are distinguishable and traceable. Image extraction process continues till the algorithm extracts all the images of from a recorded video till its end. Figs. 3.2a and 3.3a depict the clearly visible extracted images for deposition height and width respectively.

3.3 Annotation of Extracted Images

The extracted images were segregated and pre-processed by applying the sharpening kernel and convolutional filter to make them clearly visible. Last column of Table 3.2 presents number of clearly visible extracted images for each recorded video. It is evident from the last and 2nd last column of Table 3.2 that segregation and preprocessing of the extracted images reduce the number extracted images which are clearly visible as compared to the product of a recorded video duration and used image extraction rate i.e., for the recorded video no. 1, this product is 660 whereas no. of clearly visible extracted images is 470. 90% of the clearly visible extracted images were used as unannotated dataset for training and validation. Then these images were annotated using VGG image annotator which were used as labelled dataset for training and validation and the remaining 10% images were unannotated which were used in testing of the YOLO models. Figs. 3.2b and 3.3b depict annotated images for deposition height and width respectively. Each annotated image was used to compute (or predict) its deposition width, deposition height, and aspect ratio by hue saturation value (HSV) based color segmentation and centroid distance approach (or trained YOLO models) for each single-layer deposition. Subsequently, *Origin Pro 2024b* software was used to plot the variations in deposition width, height, and aspect ratio along the deposition length to detect the deposition defects namely discontinuity, non-uniformity, waviness, under-dilution and over-dilution in a single-layer deposition.

3.4 Deposition Defect Detection Methodology

Table 3.3 presents the conceptualized noble methodology for detecting different single-deposition defects in terms of discontinuous, non-uniform, wavy depositions and their different combinations (i.e., all defective depositions), their opposite combinations (i.e., all defect-free depositions), and for detecting under-dilution and over-dilution giving criterial for both their ideal and practical case. For example, in ideal case of uniform deposition, the deposition width *'w'* should remain constant along the entire deposition length *'l'* (i.e., $dw/dl = 0$). Similarly, for non-wavy and continuous depositions, change in deposition height with respect to deposition length should be equal to zero (i.e., $dh/dl = 0$), provided deposition height *'h'* is non-zero. Achieving such a level of accuracy in any AM process is not feasible. Therefore, the conceptualized methodology prescribes different criteria for ideal case and practical case of each defective and non-defective deposition. Since practical case criteria is of greater significance in solving real world problems therefore a certain level of relaxation needs to be provided to make practical defect detection approach realistic. Consequently, a variation zone of ±10% and

±5% is provided in proposed methodology for deposition width and height respectively i.e., if deposition width is 2 mm, then any variation in deposition width from 1.8 to 2.2 will be considered to be uniform deposition for all the practical purposes. Though, it is not true for discontinuous deposition because its practical and ideal criteria are same i.e., *h=0;* and/or *w=0*. Figs. 3.2c and 3.3c illustrate extracted image of discontinuous deposition and Figs. 3.2d and 3.3d show detection of discontinuous deposition when deposition width or deposition height become zero respectively.

Table 3.3: Proposed methodology for detecting defects in the single-layer depositions.

Deposition type	**Deposition defect detection criteria**		**Examples**
	Ideal case	**Practical case**	
Discontinuous deposition	$h = 0; and/or\ w = 0$	$h = 0; and/or\ w = 0$	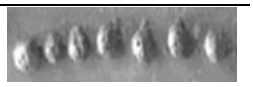
Continuous non-uniform deposition	$h \neq 0;\ w \neq 0; and\ \frac{\partial w}{\partial l} \neq 0$	$h \neq 0;\ w \neq 0; and\ \frac{\partial w}{\partial l} < 0.9w; OR\ \frac{\partial w}{\partial l} > 1.1w$	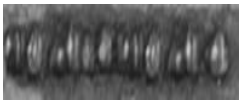
Continuous wavy deposition	$h \neq 0;\ w \neq 0; and\ \frac{\partial h}{\partial l} \neq 0$	$h \neq 0;\ w \neq 0; and\ \frac{\partial h}{\partial l} < 0.95h; OR\ \frac{\partial h}{\partial l} > 1.05h$	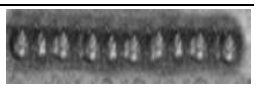
Continuous wavy non-uniform deposition	$h \neq 0;\ w \neq 0;\ \frac{\partial h}{\partial l} \neq 0;\ and\ \frac{\partial w}{\partial l} \neq 0$	$h \neq 0;\ w \neq 0; and\ \frac{\partial h}{\partial l} < 0.95h;\ OR\ \frac{\partial h}{\partial l} > 1.05h$ $\frac{\partial w}{\partial l} < 0.9w;\ OR\ \frac{\partial w}{\partial l} > 1.1w$	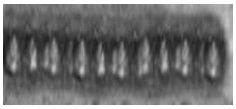
Continuous wavy uniform deposition	$h \neq 0;\ w \neq 0;\ \frac{\partial h}{\partial l} \neq 0; and\ \frac{\partial w}{\partial l} = 0$	$h \neq 0;\ w \neq 0; and\ \frac{\partial h}{\partial l} < 0.95h; OR\ \frac{\partial h}{\partial l} > 1.05h;$ $0.9w < \frac{\partial w}{\partial l} < 1.1w$	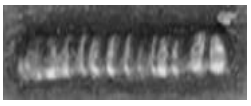
Continuous, non-wavy and non-uniform deposition	$h \neq 0;\ w \neq 0;\ \frac{\partial h}{\partial l} = 0;\ and\ \frac{\partial w}{\partial l} \neq 0$	$h \neq 0;\ w \neq 0;\ 0.95h < \frac{\partial h}{\partial l} < 1.05h; and\ \frac{\partial w}{\partial l} < 0.9w;\ OR\ \frac{\partial w}{\partial l} > 1.1w$	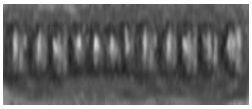
Continuous non-wavy uniform deposition	$h \neq 0;\ w \neq 0;\ \frac{\partial h}{\partial l} = 0; and\ \frac{\partial w}{\partial l} = 0$	$h \neq 0;\ w \neq 0;\ 0.95h < \frac{\partial h}{\partial l} < 1.05h; and\ 0.9w < \frac{\partial w}{\partial l} < 1.1w$	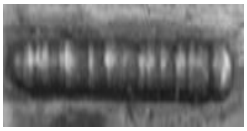
Under-dilution	$Aspect\ ratio = \frac{w}{h} < 1.3$	$Aspect\ ratio = \frac{w}{h} < 1.1$	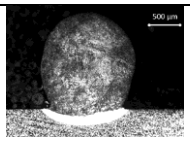
Over-dilution	$Aspect\ ratio = \frac{w}{h} > 1.8$	$Aspect\ ratio = \frac{w}{h} > 2.2$	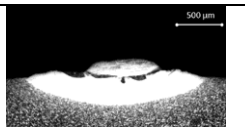
where, '*w*', '*h*', and '*l*' are the width, height, and length of a deposition respectively			

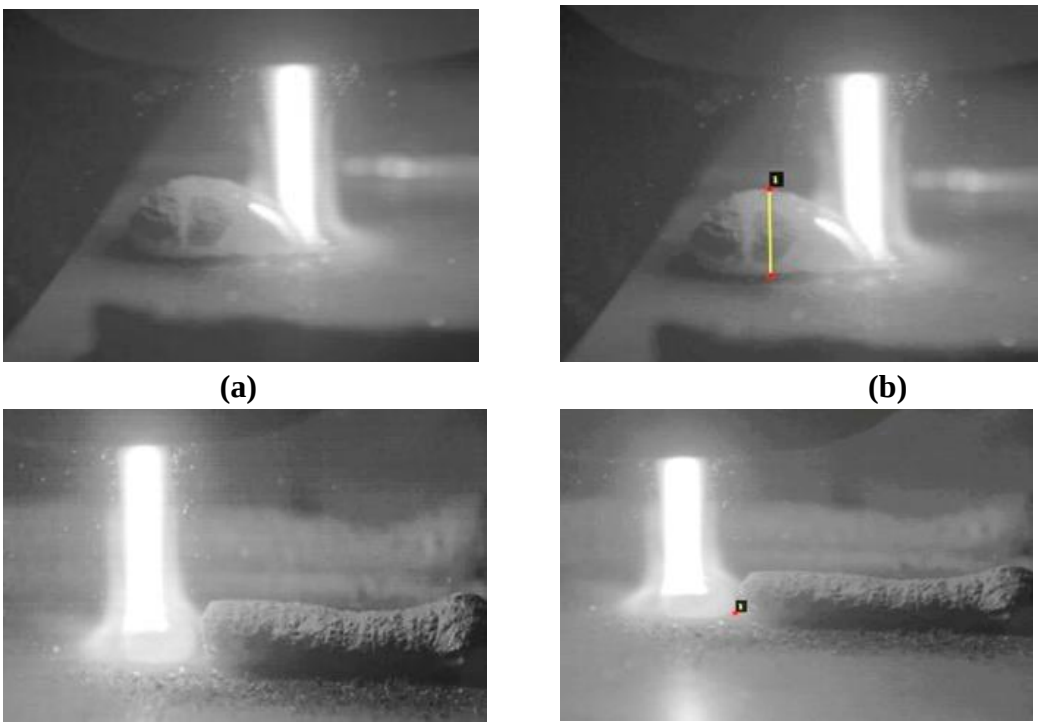

(a) **(b)**

(c) **(d)**

Fig. 3.2: Processing of a recorded video of single-layer deposition: (a) extracted image showing deposition height, (b) annotated image for computing deposition height (c) extracted image of discontinuous deposition, and (d) detection of discontinuity when deposition height becomes zero.

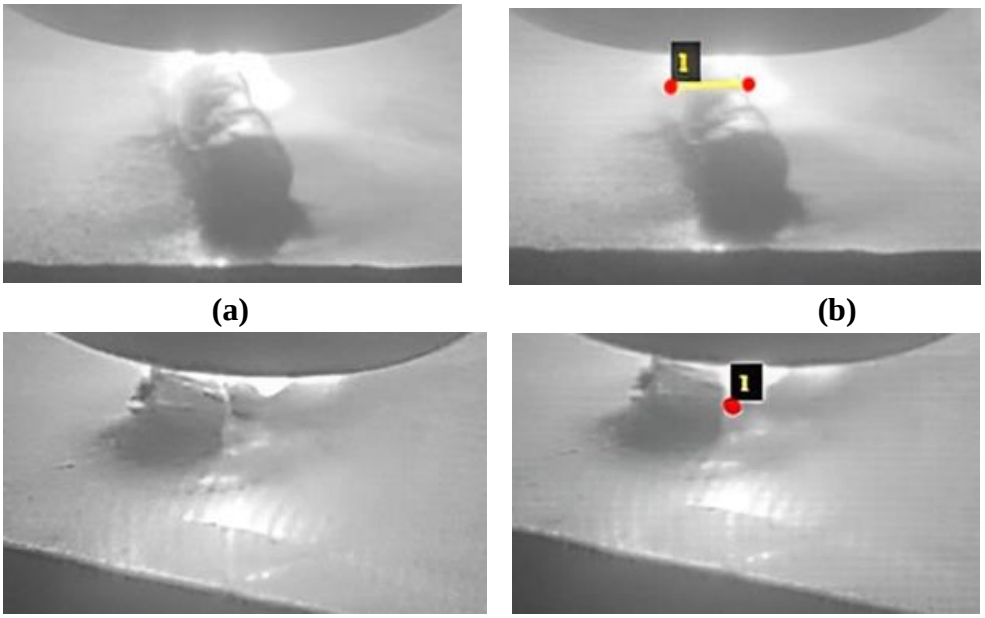

(a) **(b)**

(c) **(d)**

Fig. 3.3: Processing of a recorded video of single-layer deposition: (a) extracted image showing deposition width, (b) annotated image for computing deposition width, (c) extracted image of discontinuous deposition, and (d) detection of discontinuity when deposition width becomes zero.

3.5 Detection of Defects by HSV Segmentation and Centroid Distance

Following two approaches were used to detect the defects in single-layer depositions: approach-1 using HSV based color segmentation and centroid distance to *compute* deposition height, deposition width, and aspect ratio and approach-2 using trained YOLO models to *predict* deposition height and deposition width and compute aspect ratio. Variation in the computed/predicted values along the deposition length were used to detect discontinuity, non-uniformity, waviness, over-dilution, and under-dilution of the considered depositions.

The HSV process begins by resizing each annotated image to 830×664 pixels for better consistency and converting it to HSV color space for better red color segmentation or to detect the two red reference points as shown in Figs. 3.2b and 3.3b. The HSV color thresholds helps in finding specific colors in an image and creating the binary masks i.e., black and white contrast followed by contour analysis by figuring out shapes and edges in this contrast. Yellow line and its 2 red color end points were used to indicate the boundaries of deposition height or width in an annotated image in the present work. Then centroid of the yellow color line is found and the annotated distance between two red color boundary points having coordinates as $P\ (x_1,\ y_1)$ and $Q\ (x_2,\ y_2)$ is computed as the Euclidean distance using Eq. 3.1.

$$d = \sqrt{(x_2 - x_1)^2 + (y_2 - y_1)^2} \tag{3.1}$$

The computed distance is converted into mm using the pixel-to-mm ratio which is defined as ratio of an image resolution (usually specified in pixels e.g., 1920x1080 pixels) to camera sensor size (usually given in mm) and is given by Eq.3.2.

$$Pixel\ to\ mm\ ratio\ = \frac{Resolution\ of\ an\ image\ \ (pixels)}{Camera\ sensor\ size\ (mm)} \tag{3.2}$$

For the HDR camera used in the present work, values of pixel-to-mm ratio as 0.0375 and 0.075 were used for deposition height and width respectively. The distance found in mm is measure of deposition height or width as the case may be. Absence of yellow color line and presence of only red points is recorded as zero deposition height or width thus detecting it as discontinuous deposition. Values of deposition height obtained from all the annotated images from a recorded video are plotted as the function of time. Thereafter, deposition length is plotted as a function of time by analyzing the series of annotated images and tracking movements of red points over them for each recorded video. Length of each single-layer deposition in the present study was 50 mm and pixel to mm ratio of the HDR camera was callibrated accordingly. Then a graph showing variation in deposition height as a function of deposition length is constructed by correlating their

temporal variation graphs. Same procedure was used to construct the graph showing variation in deposition width as a function of deposition length.

3.6 Detection of Defects by YOLO Models

Detection of deposition defects by YOLO models comprises of two-step process: (i) preparation of dataset for training, validation, and testing, and (ii) use of the prepared dataset in training of YOLOv8 and YOLOv11 models and testing of the trained models.

3.6.1 Preparation of the Dataset

The annotated image and their unannotated versions were segregated into two separate folders named as *'labels'* and *'images'* respectively. Each folder contained two subfolders named as *'train'* and *'val'* which have 70% image data for training and 20% image data for validation of the YOLOv8 and YOLOv11 model respectively. Another folder named as *'test'* contained the testing data (i.e., unannotated images) for the trained YOLO models to predict deposition height and width for different single-layer depositions. Table 3.4 provides details of the images used in training, validation, and testing of YOLOv8 and YOLOv11 models for different deposition materials. The *Yet Another Markup Language (YAML)* file was used for classifying the training data into two classes for detecting deposition height and discontinuity images. Similarly, training data were classified as width and discontinuity for detecting deposition width and discontinuity images. This is a crucial step for defect detection as it takes into account information about the images and definition of classes.

Table 3.4: Details of the images used in training, validation, and testing of YOLOv8 and YOLOv11 models for different deposition materials.

Sr. No.	Feedstock material and its deposition geometry parameter	No. of images used in training	No. of images used in validation	No. of images used in testing	Total number of images
1.	Height of SS 316L	3529	1045	59	4633
2.	Width of 63Co29Cr4Mo4Ti	1020	280	72	1372
3.	Height of 63Co29Cr4Mo4Ti	2961	1085	53	4099
4.	Height of Ti6Al4V	1445	415	43	1903

3.6.2 Training and Validation of YOLO Models

Following parameters were used in the training of YOLOv8 and YOLOv11 models and their values are presented in Table 3.5:

- **Epochs:** One epoch indicates a complete reading of the entire training dataset by a YOLO model therefore number of epochs determines number of times a YOLO model reads the entire training data. Less number of epochs lead to underfitting (i.e., model is too simple to learn the underlying patterns in the training data) whereas, large number

of epochs lead to overfitting (i.e., model learns the training data too well, including noise and random fluctuations, and fails to generalize to the unseen data).

- **Batch size:** The number of images processed by a YOLO model before its weights are updated. For example, if batch size is 32 then YOLO model will process 32 images, computes loss, and update its weights. Smaller batch size leads to more frequent weight updates and less stability whereas, larger batch size results in lesser number of weight updates and usage of more memory.
- **Image resolution:** The input resolution of an image (usually in 640 × 640 pixels format) fed to a YOLO model. Larger image resolution gives better detection of smaller objects but leads to slower training of a YOLO model whereas, smaller image resolution captures less details but provides faster training to a YOLO model.
- **Learning rate:** It is the step size used in updating the weights of a YOLO model based on its training losses. Smaller learning rate leads to a slower training whereas, higher learning rate results in faster training of a YOLO model with no convergence during or at the end of the training.
- **Momentum:** It indicates the acceleration used in gradient descent by considering past gradients while updating weights of a YOLO model. It helps to avoid oscillation and speeds up the convergence. Its value is usually between 0.8 and 0.999.
- **Weight decay:** It is a regularization parameter that penalizes large weights by adding their squared values to the loss function. It prevents overfitting by constraining complexity of a YOLO model.

Table 3.5: Parameters used in the training of YOLOv8 and YOLOv11 models.

Parameters	**Values**
Epochs	50
Batch size	16
Image resolution	640
Learning rate	0.003
Momentum	0.94
Weight decay	0.0005

3.6.3 Concept of the Confusion Matrix

Confusion matrix is a performance evaluation tool for a YOLO model which is very useful for the classification problems. Fig. 3.4 depicts its concept. A confusion matrix consists of 4 quadrants and allocation of the dataset to these quadrants depends on the match between the predictions and labels. Positive and negative are the two classes, for example in the present work, deposition height and width are taken as the positive class

and discontinuity is taken as the negative class. If a positive class is predicted for a labelled negative class (i.e., height or width is predicted for discontinuity) implying false indication of a positive class therefore it is referred to as *false positive (FP)* and it is located in the 1st quadrant of the confusion matrix. If a positive class is predicted for a labelled positive class (i.e., height or width is predicted for height or width) then it is called as *true positive (TP)* and it is in the 2nd quadrant of the confusion matrix. If a negative class is predicted for a labelled positive class (i.e., discontinuity is predicted for height or width) then it gives a false indication of negative class therefore it is referred to as *false negative (FN)* and is located in 3rd quadrant of the confusion matrix. If a negative class is predicted for a labelled negative class i.e., discontinuity is predicted for discontinuity, it is referred to as true negative (TN) and it is in 4th quadrant of the confusion matrix.

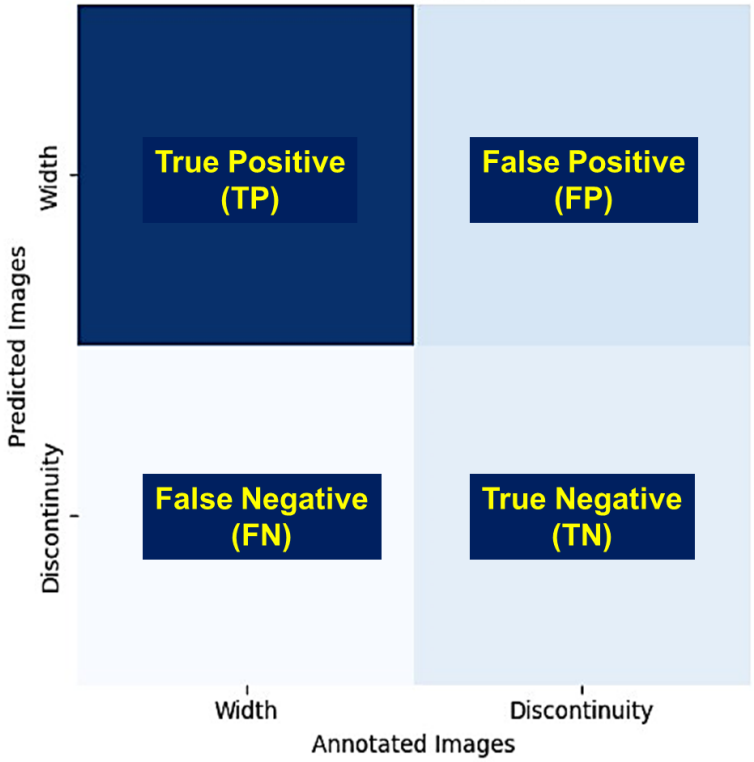

Fig. 3.4: Concept of a confusion matrix used in performance evaluation of a YOLO model.

3.6.4 Performance of the Trained YOLO Models

Following parameters were used to evaluate performance of a YOLO model:

- **Accuracy:** It indicates proportion of the correct predictions by a YOLO model. It is the ratio of sum of true positives and true negatives to the sum of true positives, true negatives, false positives, and false negatives.

$$Accuracy = \frac{TP + TN}{TP + TN + FP + FN} \qquad (3.3)$$

- **Precision:** It measures the proportion of positive identifications that are actually correct. It is defined as the ratio of true positives to the sum of true positives and false positives.

$$Precision = \frac{TP}{TP + FP} \quad (3.4)$$

- **Recall:** It is also known as true positive rate (TPR) or sensitivity. It expresses how many actual positive instances identified by a YOLO model correctly as positive or it shows how well a YOLO model can identify all positive cases. It is expressed as the ratio of true positives to the sum of true positives and false negatives.

$$Recall = \frac{TP}{TP + FN} \quad (3.5)$$

- **F1 score:** It is also called balanced F-score or F-measure. It is the most commonly used performance evaluation criterion of a classification model especially while dealing with the imbalanced datasets (i.e., where the difference between the dataset of positive and negative class is very high). It is expressed as the harmonic mean of precision and recall thus combining the two important evaluation criteria helping it to give a more comprehensive picture of a YOLO model accuracy.

$$F1\ Score = \frac{2\ x\ Precision\ x\ Recall}{Precision + Recall} \quad (3.6)$$

3.6.5 Testing of the Trained YOLO Models

The trained YOLO models were tested using only unannotated images of a single-layer deposition video (i.e., 10% of clearly visible extracted images) to predict image-wise deposition height and width. The testing process starts with a trained YOLO model accessing the file containing the trained weights for deposition height and width and processing the unannotated images from a folder named as *'test'*. Then the trained YOLO model detects the objects (i.e., deposition height or width), encloses each detected object in a green colour bounding box, predicts deposition height (or width) in pixels, and converts them to mm using pixel-to-mm a conversion factor of 0.0375 for deposition height and 0.075 for deposition width. The predicted value of deposition height (or width) is displayed in red colour text and place above the green colour bounding box. Each output image containing the bounding box and predicted value of deposition height (or width), is saved in a separate folder for further analysis. The predicted values of deposition height (or width) are plotted as the function of time and deposition length is also plotted as a function of time by analyzing the series of unannotated images. Then a graph showing variation in deposition height (or width) as a function of deposition length is constructed by correlating their temporal variation graphs.

This chapter presented details of data acquisition for the present work through high quality recording of videos of single-layer depositions of 63Co29Cr4Mo4Ti, Ti6Al4V, and SS 316L by µ-PMAM process using HDR camera. It also presented details of extraction of images from each recorded video, annotation of clearly visible extracted images, deposition defect detection methodology, and defect detection using HSV based color segmentation and centroid distance and YOLO models. The **next chapter** provides the results and discussion of this research work by describing the analysis of the deposition defects detected by HSV segmentation and centroid distance and the trained YOLO models in single-layer depositions of 63Co29Cr4Mo4Ti, Ti6Al4V, and SS 316L alloys. It also provides comparison of the ranges for deposition height, deposition width, and aspect ratio identified by HSV-based approach and the trained YOLO models and µ-PMAM process parameters identified by HSV-based approach for continuous, uniform, and non-wavy depositions of the considered materials.

Chapter 4

Results and Discussion

This chapter provides the results and discussion of this research work by describing the analysis of the deposition defects detected by HSV segmentation and centroid distance and the trained YOLO models in single-layer depositions of 63Co29Cr4Mo4Ti, Ti6Al4V, and SS 316L alloys. It also provides comparison of the ranges for deposition height, deposition width, and aspect ratio identified by HSV-based approach and the trained YOLO models and μ-PMAM process parameters identified by HSV-based approach for continuous, uniform, and non-wavy depositions of the considered materials.

4.1 Results for Single-Layer Depositions

This section presents the results and their analyses for defect detection in μ-PMAM process fabricated fifteen single-layer depositions of 63Co29Cr4Mo4Ti, four single-layer depositions of Ti6Al4V, and eight single-layer depositions of SS 316L. Discontinuity, non-uniformity, waviness, under-dilution and over-dilution have been detected using HSV colour segmentation and centroid distance-based approach and YOLO models-based approach by plotting variations in computed and predicted values of deposition height, deposition width, and aspect ratio along the deposition length. Following paragraphs describe these results.

4.1 Analysis of Defects in 63Co29Cr4Mo4Ti Depositions

15 videos were used for the analysis of defects in single-layer depositions of 63Co-29Cr-4Mo-4Ti. There were 2 approaches which were employed for the detection of defects: HSV segmentation and centroid distance, and YOLO model approach.

4.1.1 Detection of Defects by HSV Segmentation Method

Fig. 4.1 present graphs for detection of non-uniform deposition through unacceptable variation in deposition width (i.e., beyond the upper and the lower bound values of 1.38 and 1.13 mm respectively) in single-layer deposition of 63Co29Cr4Mo4Ti for 17A μ-plasma current (Fig. 4.1a) along with photographs of the obtained depositions for deposition head traverse speed of 30 mm/min (Fig. 4.1b), and 35 mm/min (Fig. 4.1c). Whereas, Fig. 4.2. shows detection of wavy deposition through unacceptable variations in 63Co29Cr4Mo4Ti single-layer depositions for different values of deposition head traverse speed and for μ-plasma current of 12A (Fig. 4.2a), 13A (Fig. 4.2b), 18A (Fig. 4.2b), 17.5A (Fig. 4.2d), and 14A and 17A for deposition head traverse speed of 40 and 45 mm/min (Fig. 4.2e).

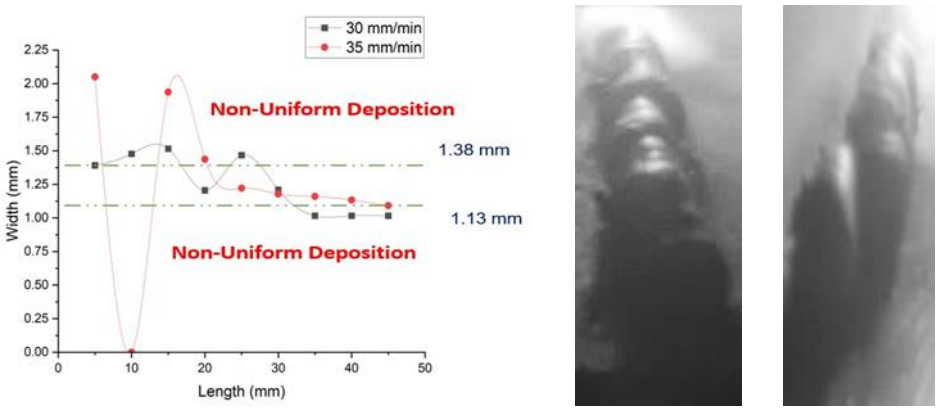

(a) **(b)** **(c)**

Fig. 4.1: (a) Detection of *non-uniform* deposition through unacceptable variation in deposition width in 63Co29Cr4Mo4Ti single-layer deposition for 17A μ-plasma current, and photograph of obtained deposition for deposition head traverse speed of (b) 30 mm/min, and (c) 35 mm/min.

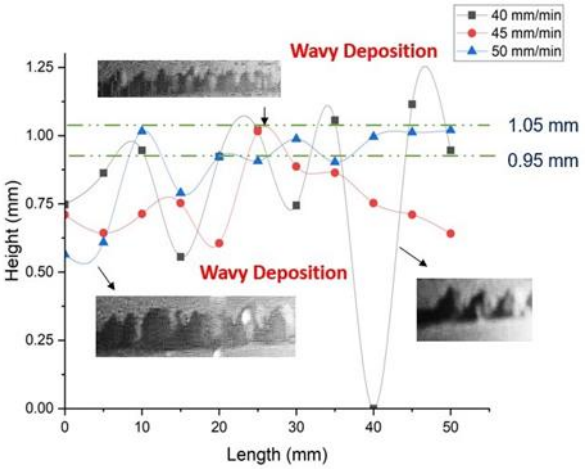

(a)

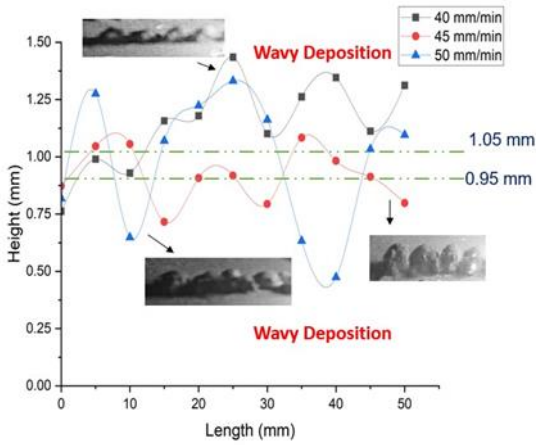

(b)

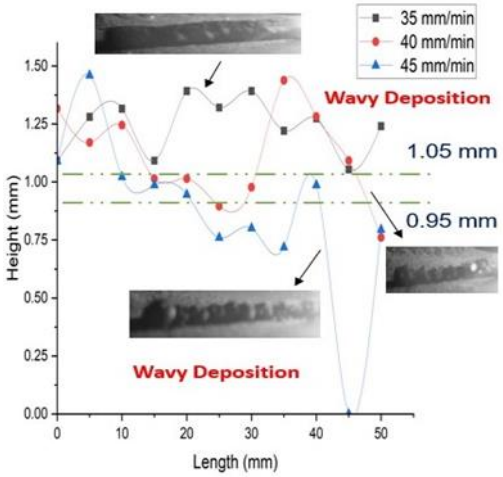

(c)

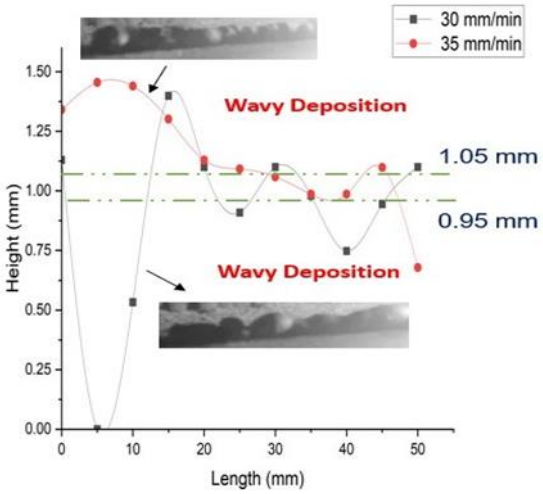

(d)

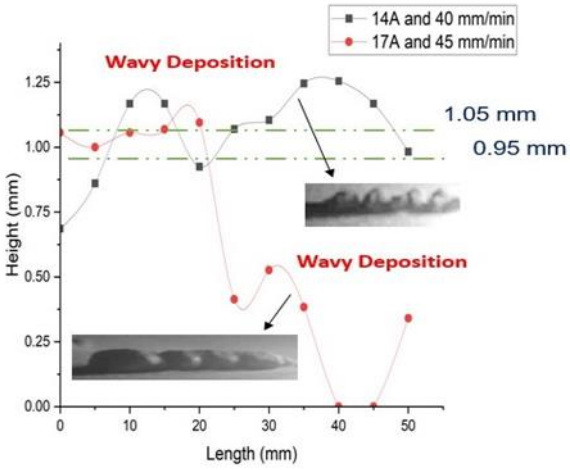

(e)

Fig. 4.2. Detection of *wavy* deposition through unacceptable variation in deposition height in 63Co29Cr4Mo4Ti single-layer depositions for different values of deposition head traverse speed and for µ-plasma current of (a) 12A, (b) 13A, (c) 18A, (d) 17.5A, and (e) 14A and 17A for deposition head traverse speed of 40 and 45 mm/min.

Following are the observations for detection of *non-uniformity* caused by variation in deposition width beyond its lower and upper bound values of 1.13 and 1.38 mm as shown in Fig. 4.1 and detection of *waviness* due to variation in deposition height beyond its lower and upper bound values of 0.95 and 1.05 mm as shown in Fig. 4.2:

- Traverse speed of deposition head of 30 mm/min gives more uniform deposition of 63Co29Cr4Mo4Ti than the deposition corresponding to 35 mm/min. It is confirmed by the corresponding deposition photographs shown in Figs. 4.1b and 4.1c. It happens because smaller traverse speed of deposition head allows the µ-plasma arc spending more interaction time with the feedstock material which results in its better melting and solidification thus giving more uniform deposition.
- Occurrence of discontinuities are observed at start of a deposition i.e., 5 mm deposition length for 17.5A µ-plasma current and 30 mm/min deposition head traverse speed (Fig. 4.2d), at 10 mm deposition length for 17A µ-plasma current and 35 mm/min traverse speed of deposition head (Fig 4.1a), and also towards the end of deposition i.e., at 40 mm deposition length for 12A µ-plasma current and 40 mm/min deposition head traverse speed (Fig. 4.2a), at 45 mm deposition length for 18A µ-plasma current and 45 mm/min deposition head traverse speed (Fig. 4.2c), and during 40-45 mm deposition length for 17A µ-plasma current and 45 mm/min deposition head traverse speed (Fig. 4.2e). It implies that proper µ-plasma arc is not formed at the start and end of single-layer depositions which may be due to (a) interrupted powder supply of feedstock material, (b) use of randomly selected process parameters, and (c) use of

dissimilar materials for feedstock and base plate. Difference in their properties cause poor metallurgical bonding between them.

- Most of the depositions are wavy for majority of their deposition length as evident form Figs. 4.2a to 4.2e. It is due to very small value of deposition height obtained in single-layer depositions of 63Co29Cr4Mo4Ti alloy which has some high melting point constituents such as Cr and Mo which cause uneven depositions.
- Waviness decreases with an increase in deposition head traverse speed for smaller µ-plasma current (Fig. 4.2a) but this trend reverses for higher µ-plasma current as shown in Figs. 4.2c 4.2b for µ-plasma current of 18A and 13A respectively.

4.1.2 Defects Detected by YOLO Models

Fig. 4.3 depicts the confusion matrix used for detection of deposition width and discontinuity images and for detection of deposition height and discontinuity images by the YOLOv8 model (Figs. 4.3a and 4.3b) and YOLOv11 (Figs. 4.3c and 4.3d) models.

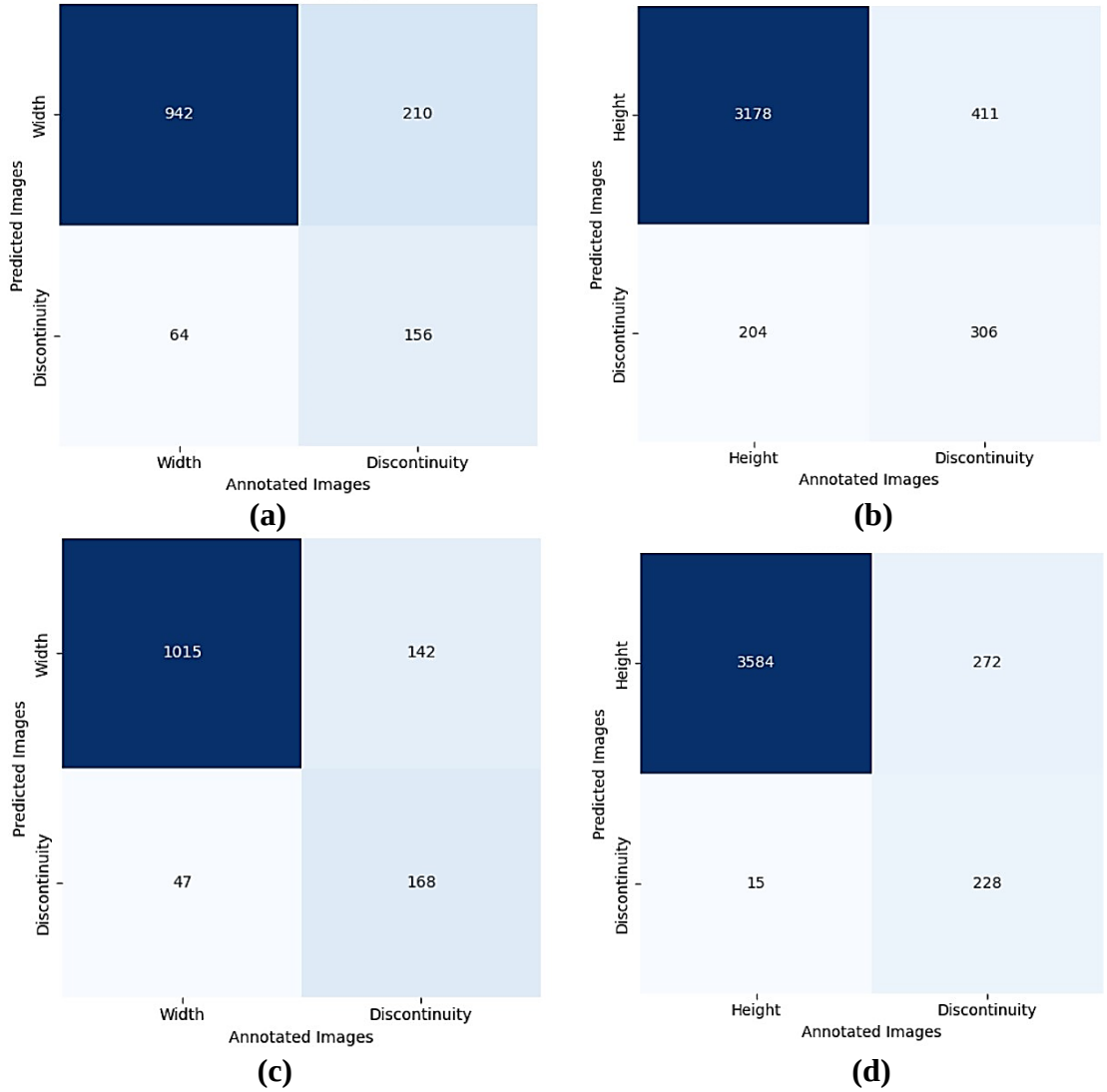

Fig. 4.3: Confusion matrix to detect deposition width and discontinuity images and deposition height and discontinuity images by (a, b) YOLOv8, and (c, d) YOLOv11.

Confusion matrix evaluates performance of a YOLO model on the basis of number of true positives, true negatives, false positives, and false negatives shown in its four quadrants. As the number of images in a quadrant increase, its color intensity also increases. It can be observed from Fig. 4.3 that both YOLOv8 and YOLOv11 models give much higher number of true positives for detecting both deposition width and discontinuity images and deposition height and discontinuity images. This proves their prediction capabilities. It can also be seen that the YOLOv11 model gives higher number of true positives for predicting both deposition width and deposition height (i.e., 1015 and 3584 images) than that given by the YOLOv8 model (i.e., 942 and 3178 images). This clearly indicates superior prediction performance of YOLOv11 than YOLOv8 model.

4.1.2.1 Performance of the Trained YOLO Models

Fig. 4.4 presents the bar diagrams showing comparison of four performance parameters namely accuracy, precision, recall, and F1 score for YOLOv8 and YOLOv11 models for the dataset of deposition width (Fig. 4.4a) and deposition height (Fig. 4.4b) of 63Co29Cr4Mo4Ti single-layer depositions. It is evident from Fig. 4.4 that the trained YOLOv11 model has higher values accuracy, precision, recall, and F1 score for the deposition width dataset (i.e., 86%; 88%; 96%; and 92% respectively) and deposition height dataset (i.e., 93%; 93%; 98%; and 95% respectively) of 63Co29Cr4Mo4Ti single-layer depositions than those corresponding to the trained YOLOv8 model (i.e., 80%; 82%; 94%; and 88% respectively for deposition width dataset and 85%; 89%; 94%; and 91% respectively for deposition height dataset). It proves superiority of YOLOv11 model than YOLOv8 model in the training performance.

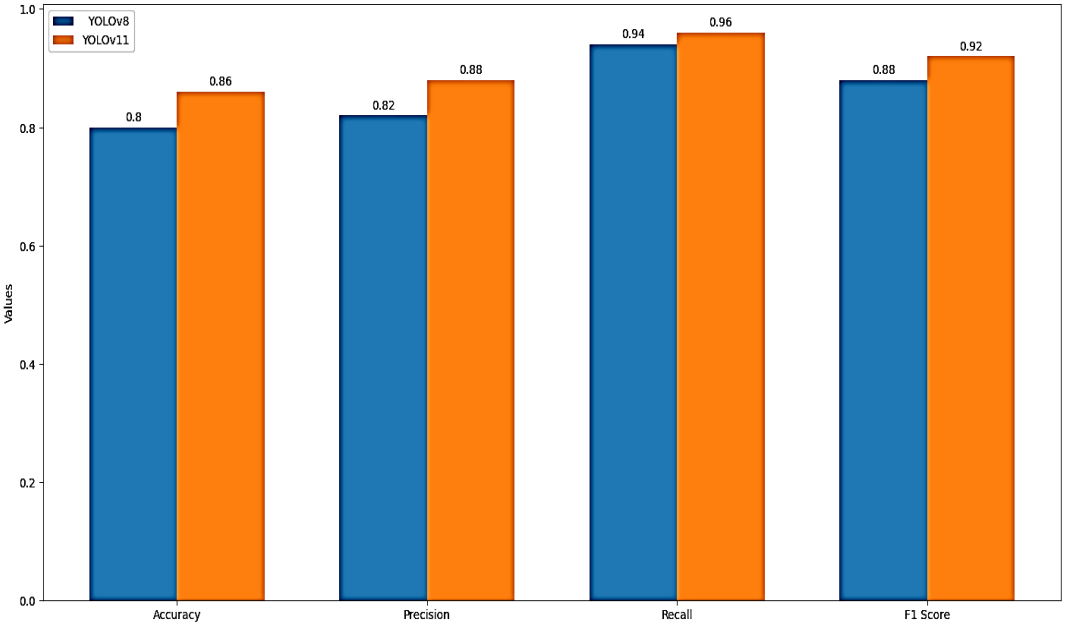

(a)

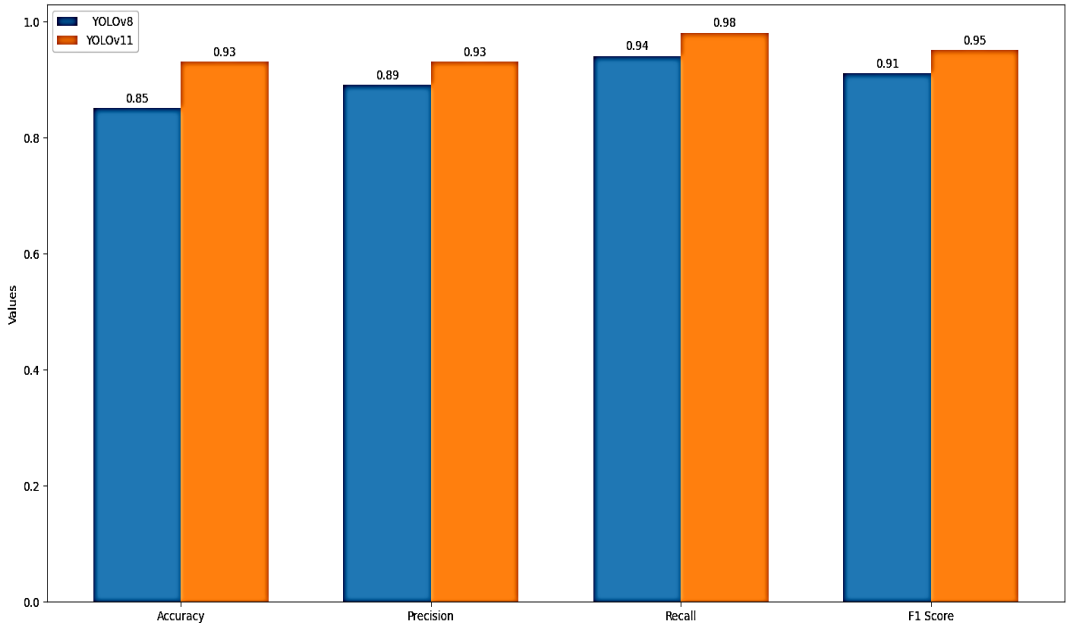

(b)

Fig. 4.4: Comparison of accuracy, precision, recall, and F1 score for YOLOv8 and YOLOv11 for 63Co29Cr4Mo4Ti single-layer deposition dataset for its (a) deposition width, and (b) deposition height.

4.1.2.2 Detection of Defects by the YOLO Models

Fig. 4.5 depicts detection of non-uniform deposition by YOLOv8 and YOLOv11 models through variation in predicted width for 63Co29Cr4Mo4Ti single-layer deposition along with computed width by HSV segmentation method. Fig. 4.6 shows photograph of an extracted image for deposition width of 63Co29Cr4Mo4Ti single-layer deposition at 54th second (Fig. 4.6a) and the width bounded by YOLOv8 model (Fig. 4.6b), and YOLOv11 model (Fig. 4.6c).

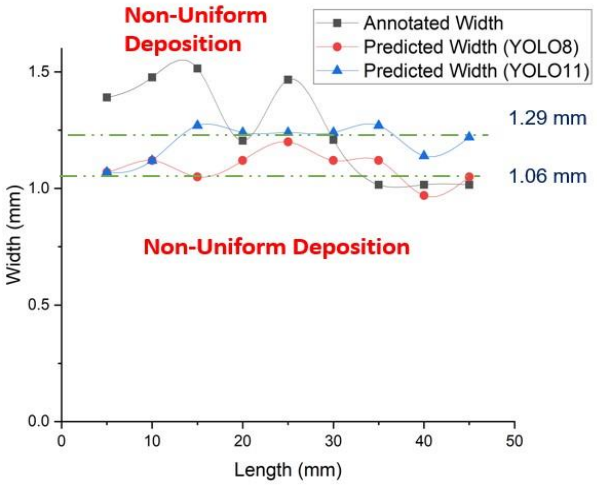

Fig. 4.5: Detection of *non-uniform* deposition by YOLOv8 and YOLOv11 models through variation in predicted width for 63Co29Cr4Mo4Ti single-layer deposition along with computed width by HSV segmentation method.

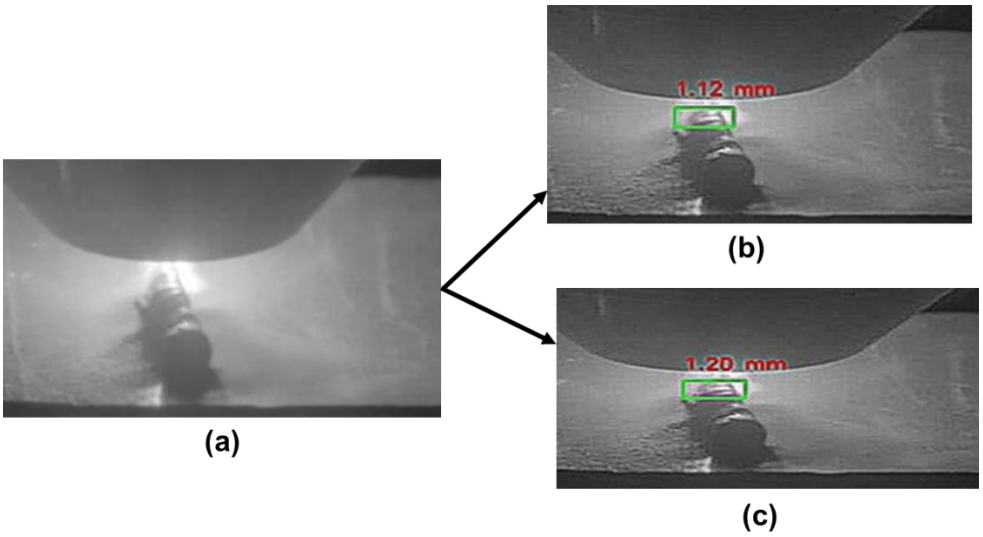

Fig. 4.6: (a) Photograph of an extracted image for deposition width of 63Co29Cr4Mo4Ti single-layer deposition at 54th second and the width bounded by (b) YOLOv8 model, and (c) YOLOv11 model.

The set of parameters that are used for predicting width are 17A current and 30 mm/min traverse speed. The upper and the lower bounds for predicted width of 63Co29Cr4Mo4Ti are 1.29 mm and 1.06 mm respectively. Width predictions generated using YOLOv8 and YOLOv11 at 54th sec are 1.12 mm and 1.20 mm respectively as shown in Fig. 4.6.

Fig. 4.7 depicts the detection of *wavy* deposition by YOLOv8, and YOLOv11 models through variation in predicted height for 63Co29Cr4Mo4Ti single-layer deposition height along with computed height by HSV segmentation method. Fig. 4.8 shows the (a) Photograph of (a) extracted image for deposition height of SS 316L single-layer deposition at 17th second (Fig. 4.8a) and the height bounded by (b) YOLOv8 model (Fig. 4.8b), and (c) YOLOv11 model (Fig. 4.8c).

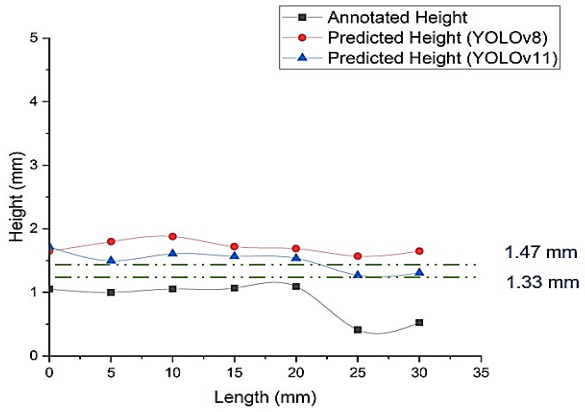

Fig. 4.7: Detection of *wavy* deposition by YOLOv8, and YOLOv11 models through variation in predicted height for 63Co29Cr4Mo4Ti single-layer deposition height along with computed height by HSV segmentation method.

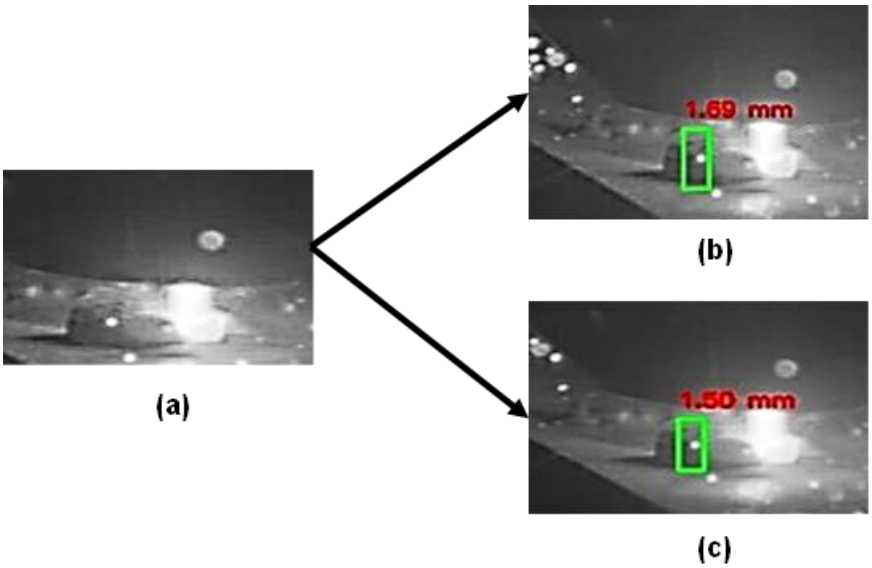

Fig. 4.8: (a) Photograph of an extracted image for deposition height of SS 316L single-layer deposition at 17th second and the height bounded by (b) YOLOv8 model, and (c) YOLOv11 model.

The set of parameters that are used for these predictions are 17A Current and 45 mm/min Traverse Speed. The upper and the lower bounds for predicted width of 63Co29Cr4Mo4Ti are 1.47 mm and 1.33 mm respectively. Height predictions generated using YOLOv8 and YOLOv11 at 17th sec are 1.69 mm and 1.50 mm respectively as shown in fig. 4.8.

4.2 Analysis of Defects in Ti6Al4V Depositions

4 videos were used for the analysis of defects in single-layer depositions of Ti6Al4V. There were 2 approaches which were employed for the detection of defects: HSV segmentation and centroid distance, and YOLO model approach.

4.2.1 Defects Detected by HSV Segmentation and Centroid Distance

Fig. 4.9. shows graphical representation for variation in deposition height along deposition length in single-layer depositions of Ti6Al4V for different set of process parameters.

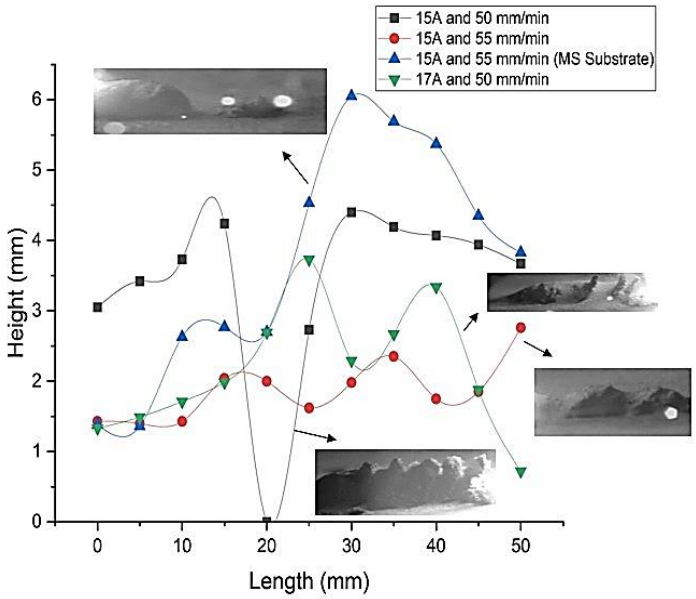

Fig. 4.9: Graphical representation for variations in deposition height along deposition length in single-layer depositions of Ti6Al4V for different set of process parameters.

Following are the observations for graphical representation for variation in deposition height along deposition length in single-layer depositions of Ti6Al4V for different set of process parameters as shown in Fig. 4.9:

- Occurrence of discontinuity is observed at 20 mm length at 15A µ-plasma current and 50 mm/min deposition head traverse speed. It can be noted that, it is found in the middle of the deposition. The possible causes for this could be (a)interrupted powder supply of the feedstock material (b) use of randomly selected process parameters.
- Due to lack of geometrical consistency, it was not possible to assign any height range for Ti6Al4V depositions. The reasons for this could be (a) random selection of process parameters i.e., unoptimized parameters.
- Maximum variation in deposition height is observed at 15A µ-plasma current and 50 mm/min deposition head traverse speed on Ti6Al4V substrate and 15A µ-plasma current and 55 mm/min deposition head traverse speed on mild steel substrate. (a) Higher µ-plasma current and traverse speed of deposition head might have led to spreading of the powder which caused this unevenness in the deposition. (b) Dissimilar materials could have caused less interaction and led to poor metallurgical bonding between the material and the substrate.
- Minimum variation in deposition height is observed at 15A µ-plasma current and 55 mm/min deposition head traverse speed on Ti6Al4V substrate. The probable causes for this could be (a) Use of similar materials for feedstock and base plate.

Similarity in their properties give proper interaction time which leads to good metallurgical bonding between them.

4.2.2 Defects Detected by YOLO Models

Fig. 4.10 depicts the confusion matrix used for detection of deposition height and discontinuity images by the YOLOv8 model (Fig. 4.10a) and YOLOv11 model (Fig. 4.10b) models.

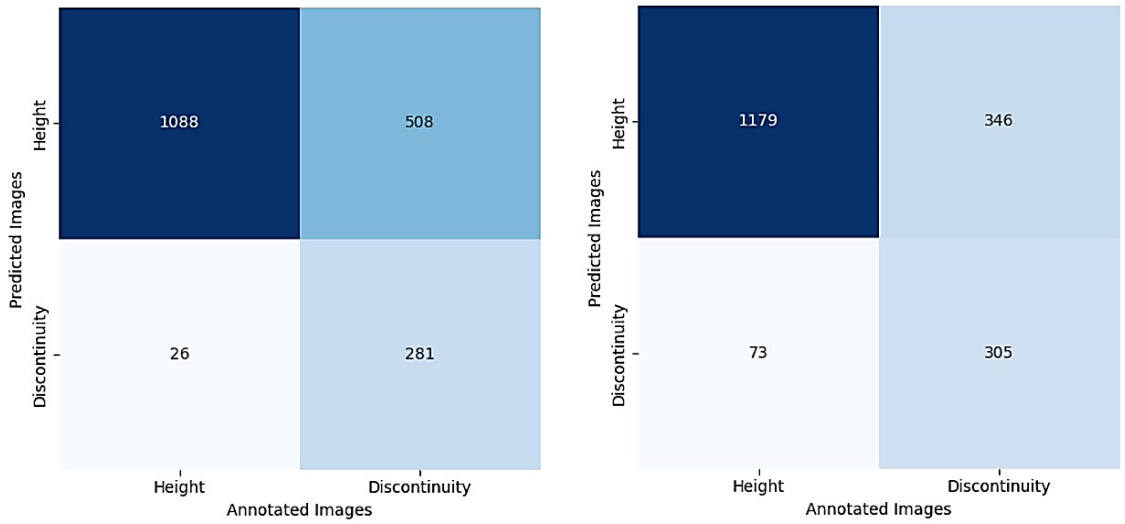

(a) **(b)**

Fig. 4.10: Confusion matrix for detection of height and discontinuity images through (a) YOLOv8 and (b) YOLOv11.

It can be observed from Fig. 4.10 that both YOLOv8 and YOLOv11 models give much higher number of true positives for detecting deposition height and discontinuity images. This proves their prediction capabilities. It can also be seen that the YOLOv11 model gives higher number of true positives and true negatives for predicting deposition height (i.e., 1179, 281 images) than given by the YOLOv8 model (i.e., 1088, 305 images). This clearly indicates superior prediction performance of YOLOv11 than YOLOv8 model.

4.2.2.1 Performance of the Trained YOLO Models

Fig. 4.11 presents the bar diagrams showing comparison of four performance parameters namely accuracy, precision, recall, and F1 score for YOLOv8 and YOLOv11 models for the dataset of deposition height of Ti6Al4V single-layer depositions.

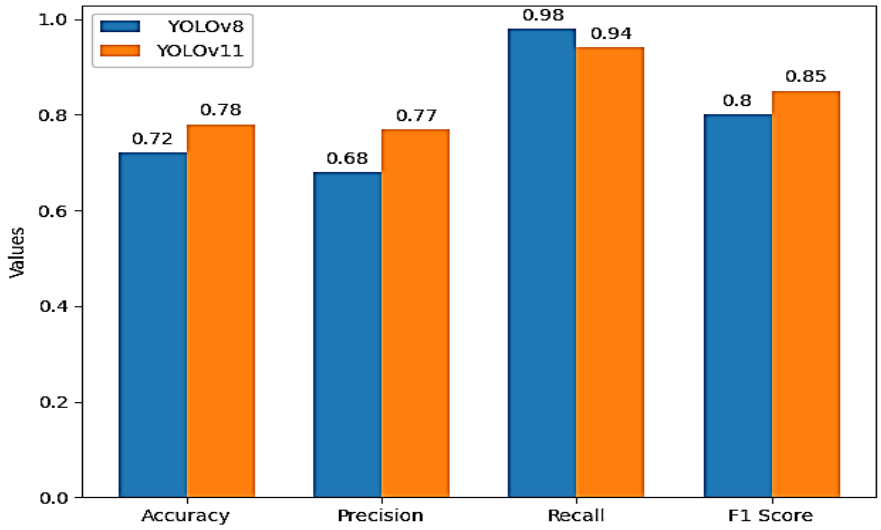

Fig. 4.11: Comparison of accuracy, precision, recall, and F1 score for YOLOv8 and YOLOv11.

It is evident from Fig. 4.11 that the trained YOLOv11 model has higher values accuracy, precision, recall, and F1 score for the deposition height dataset (i.e., 78%; 77%; 94%; and 85% respectively) of Ti6Al4V single-layer depositions than the trained YOLOv8 model (i.e., 72%; 68%; 98%; and 80%) respectively for deposition height dataset. It proves superiority of YOLOv11 model than YOLOv8 model in the training performance.

Similar observation in recall was made by **Sharma et *al*. (2024).** They found that the recall value for YOLOv8 is greater than YOLOv11. They investigated the comparative performance of speed and accuracy for YOLOv8, YOLOv9, YOLOv10, YOLOv11 and faster R-CNN algorithms. They found that large dataset could be a cause for this reverse trend in recall performance metric.

4.2.2.2 Detection of defects by the YOLO Models

Fig. 4.12 depicts the detection of waviness through annotated and predicted variation in deposition height along deposition length of Ti6Al4V single-layer depositions using HSV segmentation and centroid distance, YOLOv8, and YOLOv11. Fig 4.13 depicts the photograph of (a) extracted image for deposition height of Ti6Al4V single-layer deposition at 21st second (Fig. 4.13a) and the height bounded by (b) YOLOv8 model (Fig. 4.13b), and (c) YOLOv11 model (Fig. 4.13c).

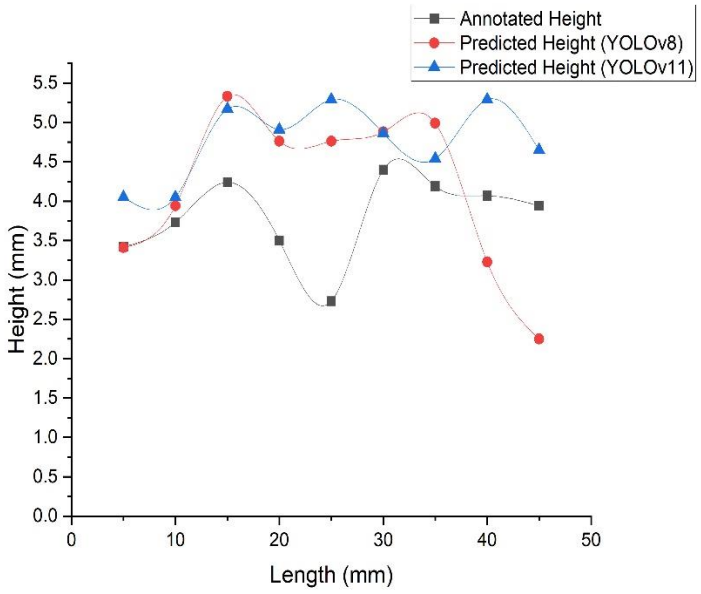

Fig. 4.12: Detection of waviness through annotated and predicted variation in deposition height along deposition length in single-layer depositions of Ti6Al4V using HSV segmentation and centroid distance, YOLOv8, and YOLOv11.

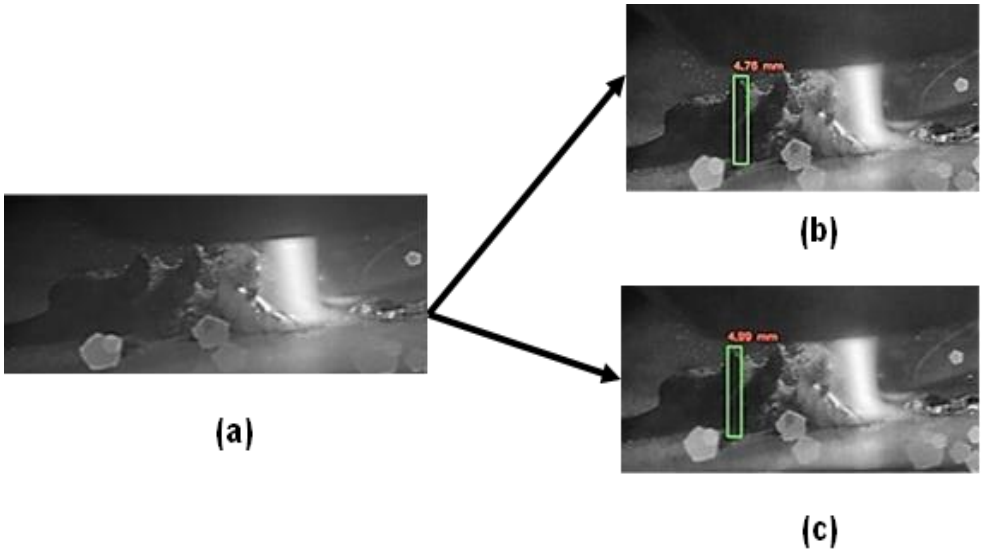

Fig. 4.13: Photograph of (a) extracted image for deposition height of Ti6Al4V single-layer deposition at 21st second and the height bounded by (b) YOLOv8 model, and (c) YOLOv11 model.

The set of parameters that are used for predicting height are 15A current and 50 mm/min traverse speed. Height predictions generated using YOLOv8 and YOLOv11 at 21st sec are 4.76 mm and 4.99 mm respectively as shown in fig. 4.13.

4.3 Analysis of defects in SS 316L depositions

8 videos were used for the analysis of defects in single-layer depositions of SS 316L. There were 2 approaches which were employed for the detection of defects: HSV segmentation and centroid distance, and YOLO model approach.

4.3.1 Defects detected by HSV segmentation and centroid distance

Fig. 4.14. depicts the detection of wavy deposition through unacceptable variation in deposition height in SS 316L single-layer depositions for different values of deposition head traverse speed and for µ-plasma current of (a) 14A, (b) 14.5A, and(c) 15A. Fig. 4.15 shows the detection of *non-uniform* deposition through unacceptable variation in deposition width in SS 316L single-layer deposition for different values of deposition head traverse speed and for µ-plasma current of (a) 14A, (b) 14.5A, and(c) 15A.

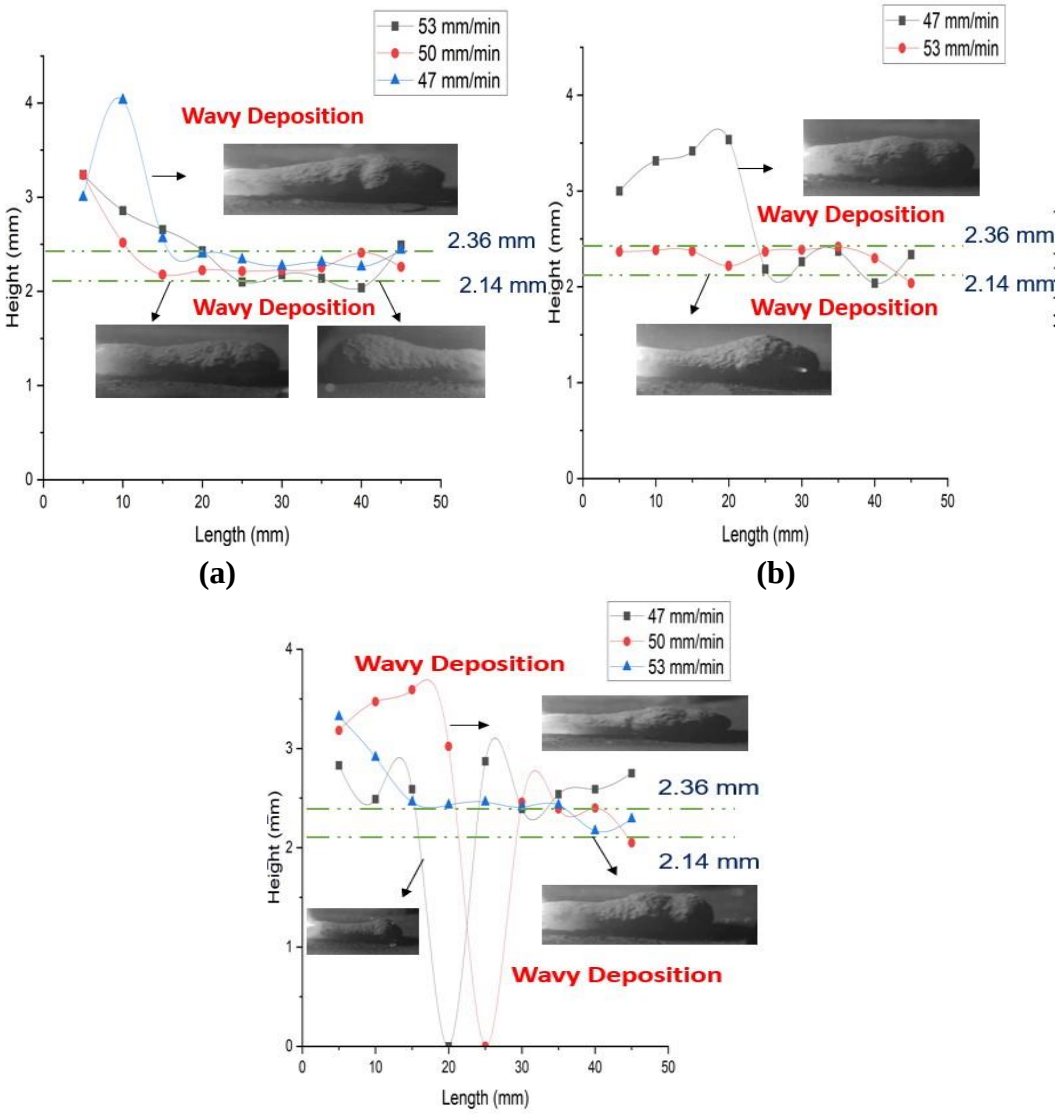

Fig. 4.14: Detection of *wavy* deposition through unacceptable variation in deposition height in SS 316L single-layer depositions for different values of deposition head traverse speed and for µ-plasma current of (a) 14A, (b) 14.5A, and(c) 15A.

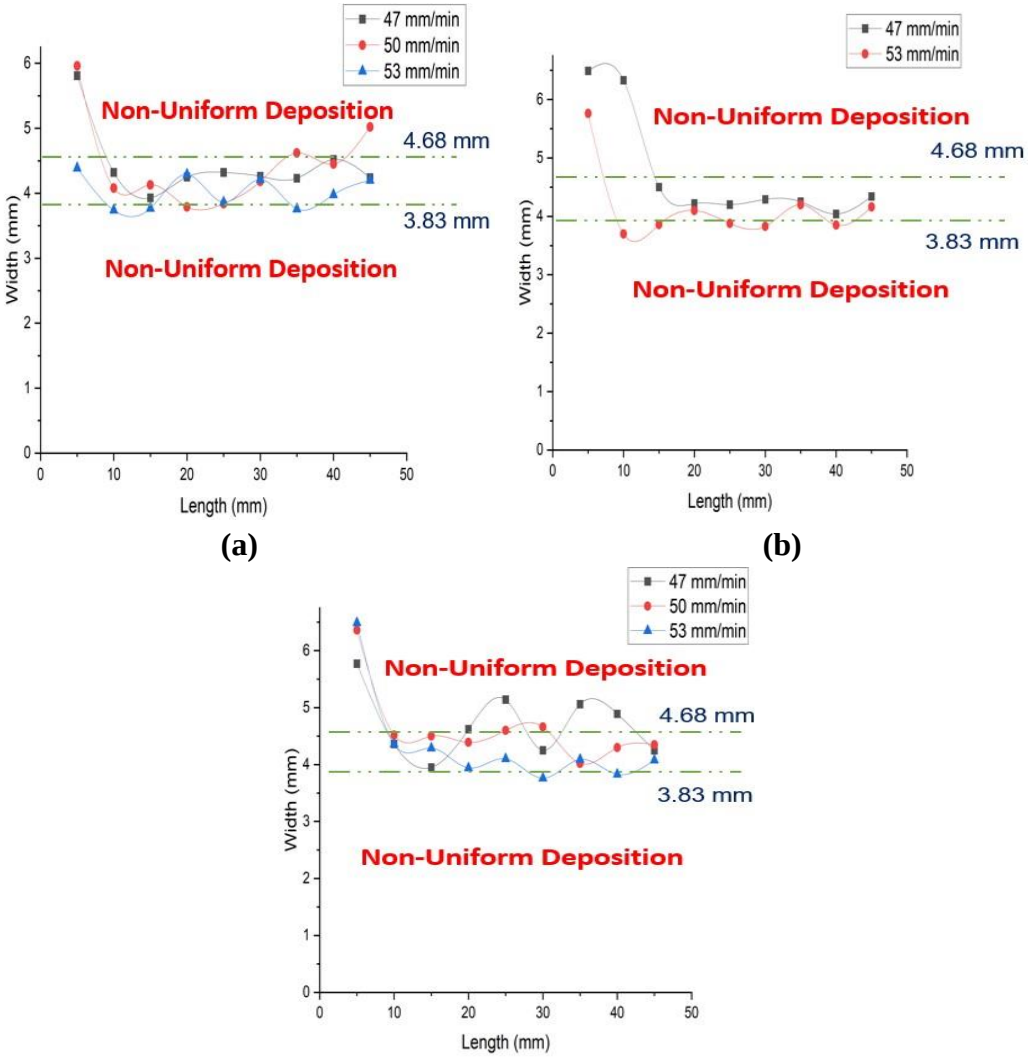

Fig. 4.15: Detection of *non-uniform* deposition through unacceptable variation in deposition width in SS 316L single-layer deposition for different values of deposition head traverse speed and for µ-plasma current of (a) 14A, (b) 14.5A, and(c) 15A.

Following are the observations for detection of *waviness* due to variation in deposition height beyond its lower and upper bound values of 2.14 and 2.36 mm as shown in Fig. 4.14 and

- At 14A and 14.5A current, deposition profile became more continuous with the increase in traverse speed as shown [fig. 4.14a, fig 4.14b]. Continuous deposition with least waviness was observed at 14.5A Current and 53 mm/min traverse speed as shown in fig. 4.14c.
- At 15A current, discontinuities were observed along with high waviness at 47 (at 20 mm length) and 50 mm/min (25 mm length). It implies that proper µ-plasma arc is not formed in the mid-deposition of single-layer depositions which may be due to (a) interrupted powder supply of feedstock material, (b) use of randomly selected process

parameters, and (c) use of dissimilar materials for feedstock and base plate. Difference in their properties cause poor metallurgical bonding between them.

- Trends clearly show that low current (14A) with moderate to high traverse speed (50 mm/min, 53 mm/min) and, high current (14.5A, 15A) with high traverse speed (53 mm/min) is essential for non-wavy depositions of SS 316L.

Post-deposition measurement of width for SS 316L depositions was done using digital vernier. Following are the observations for detection of *non-uniformity* caused by variation in deposition width beyond its lower and upper bound values of 3.83 and 4.68 mm as shown in Fig. 4.15:

- Depositions with least non uniform nature was observed for 14A current and 53 mm/min traverse speed (fig. 4.15a), and 15A current and 53 mm/min traverse speed (fig. 4.15c). At 14.5A current, uniformity is observed for lower traverse speed (47 mm/min) (fig. 4.15b). All currents (14A, 14.5A and 15A) with high traverse speed (53 mm/min) gave comparatively uniform depositions. These trends are supported by investigation of **Kotoban et *al*. (2017)**. They found that low traverse speed causes increased particle erosion, low deposition efficiency, excessive heat input, deposition defects whereas high traverse speed gives reduced erosion, higher deposition efficiency, and improved deposition quality.

Table 4.1 shows the dataset used for computation of aspect ratio variations for different combinations of µ-plasma current and deposition head traverse speed. Fig. 4.16. shows graphical representation of variations in aspect ratio of single-layer depositions of SS 316L (a) along deposition length for three values of µ-plasma current, (b) along deposition length for the entire dataset of Table 4.1, and (c) along deposition length for different combinations of µ-plasma current and deposition head traverse speed.

Table 4.1: Dataset used to compute variations in aspect ratio of single-layer depositions of SS 316L for different combinations of µ-plasma current and deposition head traverse speed.

µ-plasma current (A) and deposition head traverse speed (mm/min.)								
Data point no.	1	2	3	4	5	6	7	8
Deposition length (mm)	14/47	14/50	14/53	14.5/47	14.5/53	15/47	15/50	15/53
5	1.9	1.8	1.4	2.2	2.4	2	2	2
10	1.1	1.6	1.3	1.9	1.6	1.8	1.3	1.5
15	1.5	1.9	1.4	1.3	1.6	1.5	1.3	1.7
20	1.8	1.7	1.8	1.2	1.9	1.8	1.5	1.6
25	1.9	1.7	1.8	1.9	1.6	1.8	1.7	1.7
30	1.9	1.9	1.9	1.9	1.6	1.8	1.9	1.6
35	1.8	2.1	1.8	1.8	1.7	2	1.7	1.7
40	2	1.9	2	2	1.7	1.9	1.8	1.8
45	1.7	2.2	1.7	1.9	2	1.6	2.1	1.8

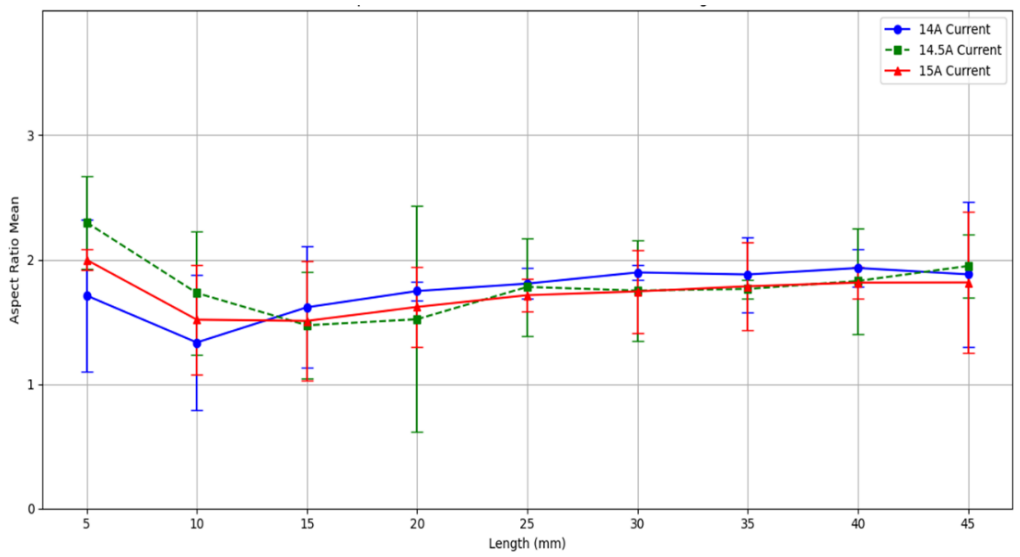

(a)

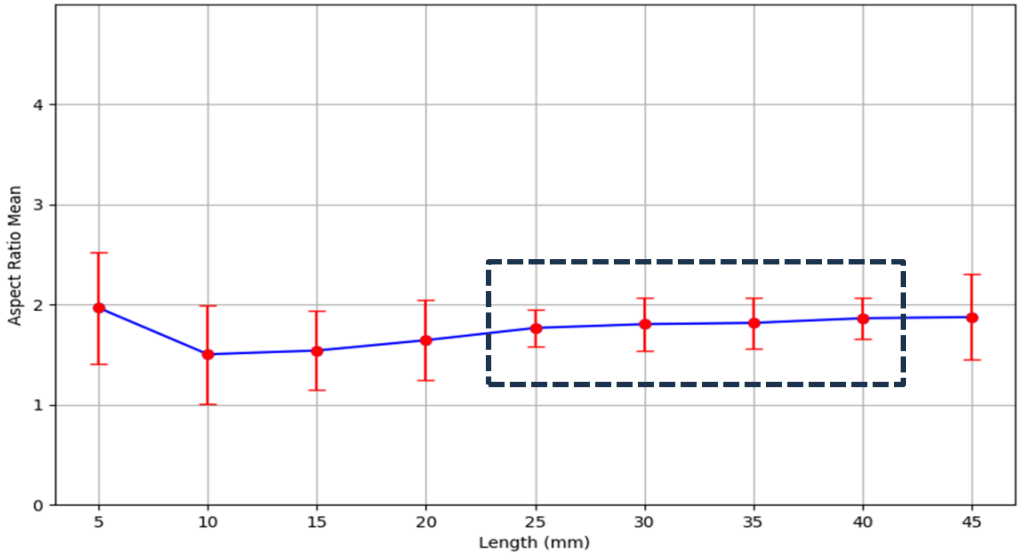

(b)

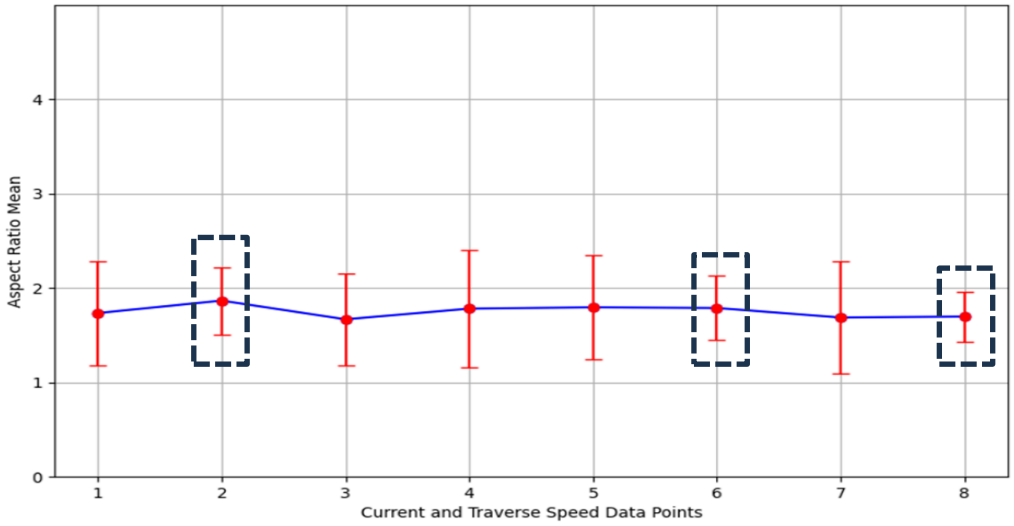

(c)

Fig. 4.16: Graphical representation of variations in aspect ratio of single-layer depositions of SS 316L (a) along deposition length for three values of µ-plasma current, (b) along

deposition length for the entire dataset of Table 4.1, and (c) along deposition length for different combinations of µ-plasma current and deposition head traverse speed.

Aspect ratio was calculated by dividing the width measured post-deposition with the height computed through HSV segmentation and centroid distance. Confidence level of 95% (z=1.96) was assumed to calculate the aspect ratios.

$$Aspect\ Ratio = \frac{Width\ Computed\ through\ Ex{-}Situ\ Measurement}{Height\ Calculated\ using\ VGG\ Annotator} \quad (4.1)$$

The dotted bounding boxes in fig. 4.16b and fig. 4.16c show that variation in aspect ratio is minimum as compared to other points in the graph. So, for fig. 4.16a, it is found that at 14A current, variation in aspect ratio is minimum at the middle of the deposition and at the end. It is found that for 14.5A current, variation in aspect ratio is lowest at a single point. It is found that for 15A current, variation in aspect ratio is least in the middle and at ends. So, for fig. 4.16b, it is found that aspect ratio variation is comparatively less for almost latter half of the deposition length. So, from fig. 4.16c, it is evident that variation in aspect ratio is minimum at random points.

Fig. 4.17 shows the detection of under-dilution and over-dilution through variation in aspect along deposition length of SS 316L single-layer depositions for a µ-plasma current of (a)14A; (b) 14.5A; and (c) 15A.

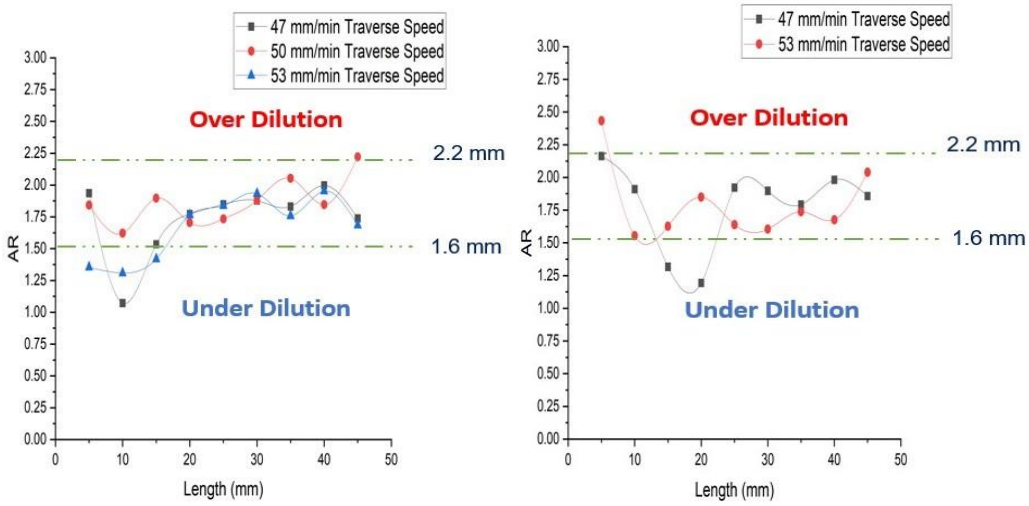

(a) **(b)**

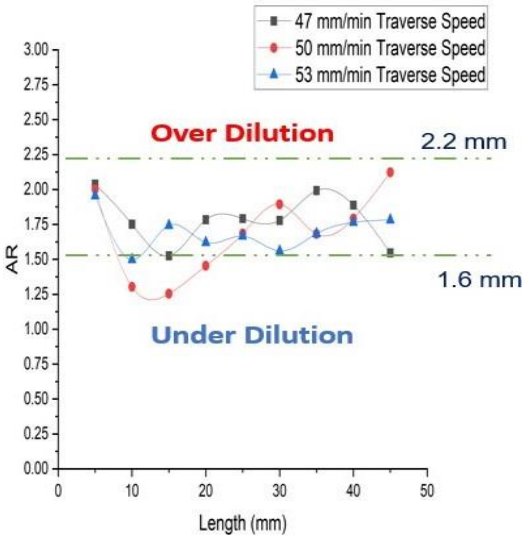

(c)

Fig. 4.17: Detection of under-dilution and over-dilution using the variation in aspect ratio along the deposition length of SS 316L single-layer depositions for a µ-plasma current of (a)14A, (b) 14.5A, and (c) 15A.

The upper and the lower bounds for aspect ratio computed using HSV segmentation and centroid distance for SS 316L are 2.2 and 1.6 respectively as show in Fig. 4.17.

4.3.2 Defects Detected by YOLO Models

Fig. 4.18. depicts the confusion matrix used for detection of deposition height and discontinuity images by the YOLOv8 model (Fig. 4.18a) and YOLOv11 model (Fig. 4.18b) models.

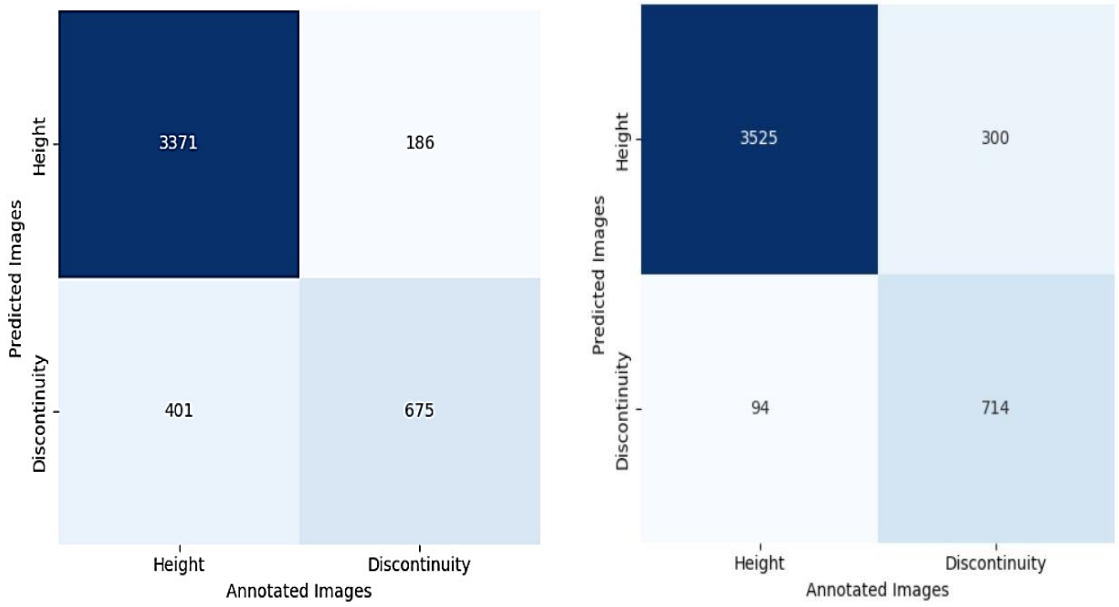

(a) **(b)**

Fig. 4.18: Confusion matrix for detection of height and discontinuity images through (a) YOLOv8 and (b) YOLOv11.

It can be observed from Fig. 4.18 that both YOLOv8 and YOLOv11 models give much higher number of true positives for detecting deposition height and discontinuity images. This proves their prediction capabilities. It can also be seen that the YOLOv11 model gives higher number of true positives and true negatives for predicting deposition height (i.e., 3371, 675 images) than given by the YOLOv8 model (i.e., 3525, 714 images). This clearly indicates superior prediction performance of YOLOv11 than YOLOv8 model.

4.3.2.1 Performance of the Trained YOLO Models

Fig. 4.19 presents the bar diagrams showing comparison of four performance parameters namely accuracy, precision, recall, and F1 score for YOLOv8 and YOLOv11 models for the dataset of deposition height of SS 316L single-layer depositions.

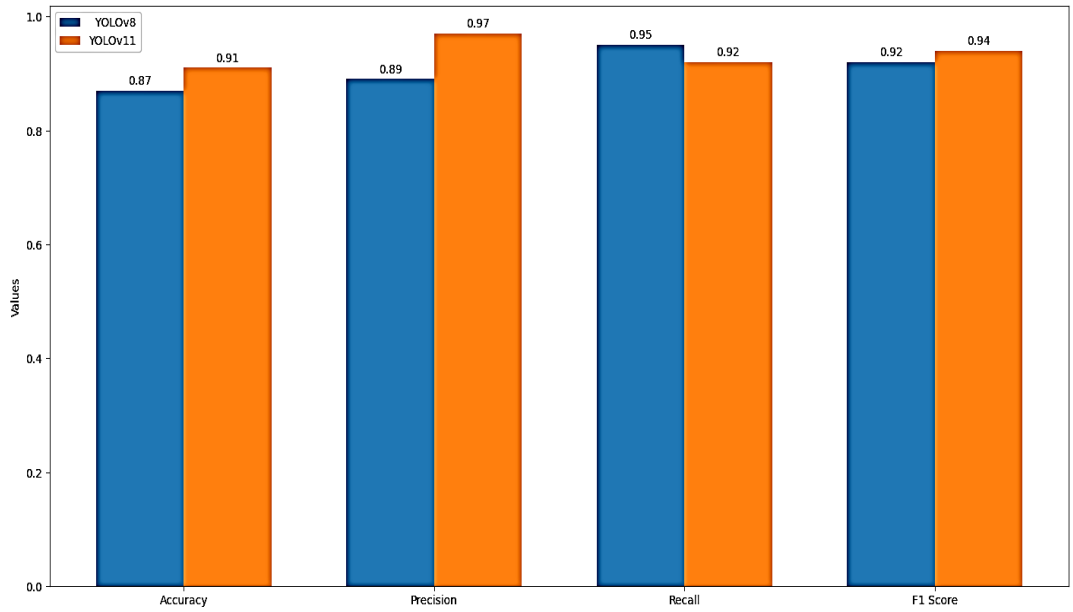

Fig. 4.19: Comparison of Accuracy, Precision, Recall, and F1 Score for YOLOv8 and YOLOv11.

It is evident from Fig. 4.19 that the trained YOLOv11 model has higher values accuracy, precision, recall, and F1 score for the deposition height dataset (i.e., 91%; 97%; 92%; and 94% respectively) of Ti6Al4V single-layer depositions than the trained YOLOv8 model (i.e., 87%; 89%; 95%; and 92%) respectively for deposition height dataset. It proves superiority of YOLOv11 model than YOLOv8 model in the training performance.

But, a reverse trend in recall metric is observed. Similar observation in recall metric was made by **Sharma et *al.* (2024).** They found that the recall value for YOLOv8 is greater than YOLOv11. They investigated the comparative performance of speed and accuracy for YOLOv8, YOLOv9, YOLOv10, YOLOv11 and faster R-CNN algorithms.

They found that large dataset could be a cause for this reverse trend in recall performance metric.

4.3.2.2 Detection of defects by the YOLO Models

Fig. 4.20 depicts the detection of waviness, under-dilution and over-dilution through variation in deposition height and aspect along deposition length of SS 316L single-layer depositions using HSV segmentation and centroid distance, YOLOv8, and YOLOv11. Fig 4.21 depicts the photograph of (a) extracted image for deposition height of SS 316L single-layer deposition at 44th second (Fig. 4.21a) and the height bounded by (b) YOLOv8 model (Fig. 4.21b), and (c) YOLOv11 model (Fig. 4.21c).

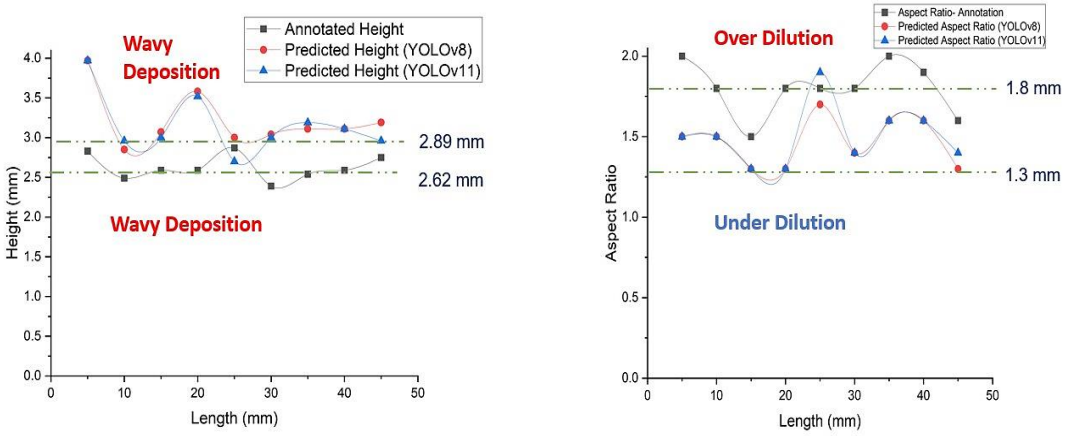

(a) **(b)**

Fig. 4.20: Detection of waviness, under-dilution, and over-dilution through variation in deposition height and aspect along deposition length of SS 316L single-layer depositions using HSV segmentation and centroid distance, YOLOv8, and YOLOv11.

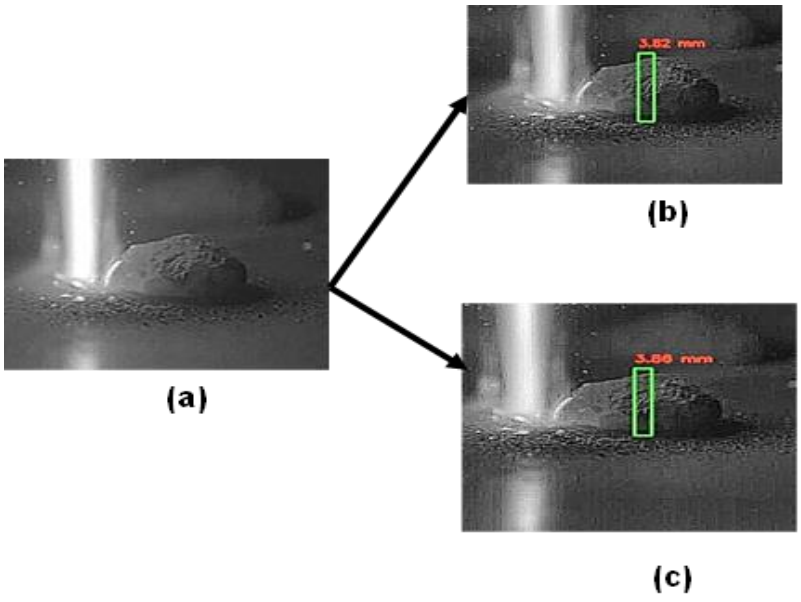

Fig. 4.21: Photograph of (a) extracted image for deposition height of SS 316L single-layer deposition at 44th second and the height bounded by (b) YOLOv8 model, and (c) YOLOv11 model.

The upper and the lower bounds for height of SS 316L are 2.89 mm and 2.62 mm respectively. The upper and the lower bounds for aspect ratio of SS 316L are 1.8 mm and 1.3 mm respectively. The set of parameters that are used for these predictions are 15A µ-plasma current and 47 mm/min traverse speed. Height predictions generated using YOLOv8 and YOLOv11 at 44th sec are 3.82 mm and 3.86 mm respectively as shown in fig. 4.21.

4.5 Comparison of Identified Process Parameters and Deposition Geometry Ranges by HSV and YOLO Models

Table 4.2 presents comparison of ranges for deposition width, deposition height, and aspect ratio identified by HSV and centroid distance-based approach and YOLO models for single-layer depositions of SS 316L and 63Co29Cr4Mo4Ti along with µ-PMAM process parameters identified HSV and centroid distance-based approach for their continuous and non-wavy, and uniform depositions.

Table 4.2: HSV and YOLO models identified ranges for deposition geometry parameters for SS 316L and 63Co29Cr4Mo4Ti single-layer depositions and along with µ-PMAM process parameters identified by HSV approach for their continuous and non-wavy, and uniform depositions.

Feedstock material	**Defect detection approach**	**Identified range for width**	**Identified range for height**	**Identified range for aspect ratio**	**Identified parameters of µ-PMAM process**			
					µ-plasma current (A)	Deposition head traverse speed (mm/min)	µ-plasma current (A)	Deposition head traverse speed (mm/min)
SS 316L	HSV and centroid distance-based approach	3.83-4.68	2.14-2.36	1.6-2.2	For non-wavy and continuous deposition		For uniform deposition	
					14.5	53	14.5	53
	YOLO models	3.83-4.68	2.62-2.89	1.3-1.8	NA	NA	NA	NA
63Co29Cr4Mo4Ti	HSV and centroid distance-based approach	1.13-1.38	0.95-1.05	1.1–1.5	For non-wavy and continuous deposition		For uniform deposition	
					13	45	17	30
					14	40		
	YOLO models	1.06-1.29	1.33-1.47	0.7- 1.0	NA	NA	NA	NA

This chapter presented the results and discussion of this research work by describing the analysis of the deposition defects detected by HSV segmentation and centroid distance and the trained YOLO models in single-layer depositions of SS 316L, Ti6Al4V, and 63Co29Cr4Mo4Ti alloys. It also provides comparison of the ranges for deposition height, deposition width, and aspect ratio identified by HSV-based approach and the trained

YOLO models and μ-PMAM process parameters identified by HSV-based approach for continuous, uniform, and non-wavy depositions of the considered materials. The **next chapter** will summarize the outcome of the present research by presenting its significant achievements, conclusions, and some directions for the future work.

Chapter 5

Conclusions and Scope for Future Work

This chapter summarizes the outcome of the present research by presenting its significant achievements, conclusions, and some directions for the future work.

5.1 Significant Achievements

Significant achievements of the present work that are worth mentioning include:

- Implementation of computer vision techniques, specifically using HSV segmentation and centroid distance, YOLOv8, and YOLOv11 for real-time defect detection in the µ-PMAM process.
- Detection and classification of key deposition defects such as discontinuity, waviness, non-uniformity, under-dilution, and over-dilution using HSV segmentation and centroid distance.
- Detection and classification of key deposition defects such as waviness, non-uniformity, under-dilution, and over-dilution using YOLOv8 and YOLOv11. Prediction of deposition width and deposition height using YOLOv8 and YOLOv11.
- Computation of width, height, and aspect ratio ranges using HSV segmentation and centroid distance, YOLOv8, and YOLOv11 for single-layer depositions of SS 316L and 63Co29Cr4Mo4Ti.

5.2 Conclusions

- Comparative analysis across SS 316L, 63Co29Cr4Mo4Ti, and Ti6Al4V materials provided valuable insights into process parameters for uniform and continuous depositions. In case of Ti6Al4V, as the deposition height lacked consistency, it was not possible to assign any range for it.
- Trends clearly show that low µ-plasma current (14A) with moderate to high traverse speed (50 mm/min, 53 mm/min) and, high µ-plasma current (14.5A, 15A) with high traverse speed (53 mm/min) of deposition head is essential for non-wavy depositions of SS 316L. All currents (14A, 14.5A and 15A) with high deposition head traverse speed (53 mm/min) gave comparatively uniform depositions.
- Low µ-plasma current and high deposition head traverse speed are essential for uniform 63Co29Cr4Mo4Ti depositions. Upon increasing the current, low to moderate deposition head traverse speed parameters yielded non- wavy 63Co29Cr4Mo4Ti

depositions. So, it can be concluded that low to moderate deposition head traverse speed is essential for fabricating 63Co29Cr4Mo4Ti non- wavy depositions.

- Highest accuracy was obtained for height detection of 63Co29Cr4Mo4Ti material (93%) using YOLOv11. Highest precision was achieved for height detection of SS 316L material (97%) on YOLOv11. Highest recall was obtained for height detection of Ti6Al4V material (98%) using YOLOV11 and height detection of 63Co29Cr4Mo4Ti material (98%) on YOLOv8. Highest F1 score was achieved for height detection of 63Co29Cr4Mo4Ti material (95%) through YOLOv11.

5.3 Scope for Future Work

- This research can be taken further to study various defects that occur between the layers and, between layer and substrate for multi-layer and multi-track depositions.
- For single-layer depositions, this study can be extended to different kinds of materials deposited using additive manufacturing processes.
- The scope of defect detection can also be broadened to different defects such as surface roughness and delamination.
- Different models such as R-CNN can be used to train the dataset to analyze the depositions.
- A digital twin system can be developed by integrating the defect detection system with the parameter optimization techniques. Currently, it is in the digital shadow phase of development.

References

Arya PK, Jain NK, Sathiaraj D (2024). Microstructure and mechanical properties of additively manufactured Ti6Al4VxCryNi alloy. ***CIRP J Manuf Sci Technol,*** 53: 67-80. https://doi.org/10.1016/j.cirpj.2024.07.001

Bourell DL (2016). Perspectives on Additive Manufacturing. ***Annu Rev Mater Res,*** 46:1–18. https://doi.org/10.1146/annurev-matsci-070115-031606

Charalampous P, Kostavelis I, Kopsacheilis C, Tzovaras D (2021). Vision-based real-time monitoring of extrusion additive manufacturing processes for automatic manufacturing error detection. ***Int J Adv Manuf Technol,*** 115:3859–3872**.** https://doi.org/10.1007/s00170-021-07419-2

Cunha NA, Inocêncio AV de M, Cavalcante EL, et *al.* (2024). Computer vision: applications in biomedical engineering. ***Caderno Pedagógico,*** 21**,** e11502. https://doi.org/10.54033/cadpedv21n13-056

DeCost BL, Holm EA (2015). A computer vision approach for automated analysis and classification of microstructural image data**.** ***Comput Mater Sci,*** 110:126–133. https://doi.org/10.1016/j.commatsci.2015.08.011

Diwan T, Anirudh G, Tembhurne JV (2023). Object detection using YOLO: challenges, architectural successors, datasets and applications. ***Multimed Tools Appl,*** 82:9243–9275. https://doi.org/10.1007/s11042-022-13644-y

Gargiulo P, Árnadóttir Í, Gíslason M, Edmunds K, Ólafsson, I (2017). New directions in 3D medical modeling: 3D-printing anatomy and functions in neurosurgical planning. ***J Healthc Eng,*** **2017:1–8.** https://doi.org/10.1155/2017/1439643

Jadhav A, Jadhav VS (2022). A review on 3D printing: An additive manufacturing technology. ***Mater Today Proc,*** 62:2094–2099. https://doi.org/10.1016/j.matpr.2022.02.558

Jhavar S, Jain NK, Paul CP (**2014**). Enhancement of deposition quality in microplasma transferred arc deposition process. ***Mater Manuf Processes***, 29(8): 1017-1023, https://doi.org/10.1080/10426914.2014.892984

Jhavar S, Jain NK, Paul CP (**2016**). Micro-plasma transferred arc additive manufacturing for die and mold surface remanufacturing. ***JOM***, 68(7): https://doi.org/10.1007/s11837-016-1932-z

Kotoban D, Grigoriev S, Okunkova A, Sova A (2017). Influence of a shape of single track on deposition efficiency of 316L stainless steel powder in cold spray. **Surf Coat Technol,** 309:951–958. https://doi.org/10.1016/j.surfcoat.2016.10.052

Kumar P, Jain NK (2020). Effect of material form on deposition characteristics in micro-plasma transferred arc additive manufacturing process. ***CIRP J Manuf Sci Technol,*** 30:195–205. https://doi.org/10.1016/j.cirpj.2020.05.008

Kumar P, Jain NK (2022). Surface roughness prediction in micro-plasma transferred arc metal additive manufacturing process using K-nearest neighbors algorithm. ***Int J Adv Manuf Technol,*** 119:2985–2997. https://doi.org/10.1007/s00170-021-08639-2

Lin TH, Yang CY, Shih WP (2017). Fall prevention shoes using camera-based line-laser obstacle detection system. ***J Healthc Eng,*** 2017, e264071. https://doi.org/10.1155/2017/8264071

Nguyen NV, Hum AJW, Do T, Tran T (2023). Semi-supervised machine learning of optical *in-situ* monitoring data for anomaly detection in laser powder bed fusion.

Virtual Phys Prototyp, 18, e2129396. https://doi.org/10.1080/17452759.2022.2129396

Scime L, Beuth J (2018). Anomaly detection and classification in a laser powder bed additive manufacturing process using a trained computer vision algorithm. ***Addit Manuf,*** 19:114–126. https://doi.org/10.1016/j.addma.2017.11.009

Scime L, Siddel D, Baird S, Paquit V (2020). Layer-wise anomaly detection and classification for powder bed additive manufacturing processes: A machine-agnostic algorithm for real-time pixel-wise semantic segmentation. ***Addit Manuf,*** 36, 101453. https://doi.org/10.1016/j.addma.2020.101453

Sharma A, Kumar V, Longchamps L (2024). Comparative performance of YOLOv8, YOLOv9, YOLOv10, YOLOv11 and faster R-CNN models for detection of multiple weed species. ***Smart Agric Technol,*** 9, 100648. https://doi.org/10.1016/j.atech.2024.100648

Stavropoulos P, Foteinopoulos P (2018). Modelling of additive manufacturing processes: a review and classification. **Manuf Rev (Les Ulis),** 5, 2. https://doi.org/10.1051/mfreview/2017014

Vijayakumar A, Vairavasundaram S (2024). YOLO-based object detection models: A review and its applications. ***Multimed Tools Appl,*** 83:83535–83574. https://doi.org/10.1007/s11042-024-18872-y

Wang SY, Zhang PZ, Zhou SY, Wei DB, Ding F, Li FK (2020). A computer vision based machine learning approach for fatigue crack initiation sites recognition. ***Comput Mater Sci,*** 171, 109259. https://doi.org/10.1016/j.commatsci.2019.109259

Wang W, Wang P, Zhang H, et *al.* (2023). A real-time defect detection strategy for additive manufacturing processes based on deep learning and machine vision technologies. ***Micromachines,*** 15(1), 28. https://doi.org/10.3390/mi15010028

Wiberg A (2021) *Design Automation for Additive Manufacturing: A Multi-Disciplinary Optimization Approach*. Linköping University Electronic Press, Linköping. 31247715. https://doi.org/10.3384/9789179291082

Zhang Y, Shen S, Li H, Hu Y (2022). Review of in-situ and real-time monitoring of metal additive manufacturing based on image processing. ***Int J Adv Manuf Technol,*** 123:1-20. https://doi.org/10.1007/s00170-022-10178-3